

The chemical structure of young high-mass star-forming clumps: (I) Deuteration*

S. FENG (CHINESE NAME),^{1,2,3} P. CASELLI,⁴ K. WANG (CHINESE NAME),⁵ Y. LIN (CHINESE NAME),⁶ H. BEUTHER,⁷ AND O. SIPILÄ⁴

¹National Astronomical Observatory of China, Datun Road 20, Chaoyang, Beijing, 100012, P. R. China

²CAS Key Laboratory of FAST, NAOC, Chinese Academy of Sciences, P. R. China

³National Astronomical Observatory of Japan, 2 Chome-21-1 Osawa, Mitaka-shi, Tokyo-to 181-8588, Japan

⁴Max-Planck-Institut für Extraterrestrische Physik, Gießenbachstraße 1, D-85748, Garching bei München, Germany

⁵Kavli Institute for Astronomy and Astrophysics, Peking University, 5 Yiheyuan Road, Haidian District, Beijing 100871, China

⁶Max Planck Institute for Radio Astronomy, Auf dem Hügel 69, D-53121 Bonn, Germany

⁷Max-Planck-Institut für Astronomie, Königstuhl 17, D-69117, Heidelberg, Germany

(Received; Revised; Accepted 2019 Aug. 10)

Submitted to ApJ

ABSTRACT

The chemical structure of high-mass star nurseries is important for a general understanding of star formation. Deuteration is a key chemical process in the earliest stages of star formation because its efficiency is sensitive to the environment. Using the IRAM-30 m telescope at 1.3–4.3 mm wavelengths, we have imaged two parsec-scale high-mass protostellar clumps (P1 and S) that show different evolutionary stages but are located in the same giant filamentary infrared dark cloud G28.34+0.06. Deep spectral images at subparsec resolution reveal the dust and gas physical structures of both clumps. We find that (1) the low- J lines of N_2H^+ , HCN, HNC, and HCO^+ isotopologues are subthermally excited; and (2) the deuteration of N_2H^+ is more efficient than that of HCO^+ , HCN, and HNC by an order of magnitude. The deuteration of these species are enriched toward the chemically younger clump S compared with P1, indicating that this process favors the colder and denser environment ($T_{\text{kin}} \sim 14\text{K}$, $N(\text{NH}_3) \sim 9 \times 10^{15} \text{cm}^{-2}$). In contrast, single deuteration of NH_3 is insensitive to the environmental difference between P1 and S; and (3) single deuteration of CH_3OH ($> 10\%$) is detected toward the location where CO shows a depletion of ~ 10 . This comparative chemical study between P1 and S links the chemical variations to the environmental differences and shows chemical similarities between the early phases of high- and low-mass star-forming regions.

Keywords: ISM: abundances; ISM: lines and bands; ISM: molecules; Stars: formation; Stars: massive

1. INTRODUCTION

Unlike high-mass protostellar sources, which are characterized by a high temperature and rich spectra, dense regions ($n \geq 10^3 - 10^5 \text{cm}^{-3}$) where protostellar objects have not yet formed are less well characterized (e.g., Teyssier et al. 2002; Rathborne et al. 2006; Butler & Tan 2009; Ragan et al. 2009). The main reason for this is the low temperature ($T < 20 \text{K}$, e.g., Sridharan et al. 2005; Pillai et al. 2006; Wang et al. 2008; Wienen et al. 2012; Chira et al. 2013), which translates into a lower degree of excitation in gas-phase molecular lines. In low-mass prestellar cores and high-mass starless

cores (cores have the mass reservoir to form a high-mass star in the prestellar phase, McKee & Tan 2003; Tan et al. 2014), heating or feedback activities are not present, so the signatures of the early kinematic and chemical properties are not yet destroyed. Therefore, the natal molecular clouds, which harbor low-mass prestellar cores, high-mass starless cores, as well as high-mass young stellar objects, usually have low luminosity, showing high dust extinction even at $70 \mu\text{m}$ wavelength (e.g., Ragan et al. 2012, 2013). The so-called infrared dark clouds (IRDCs, e.g., Cyganowski et al. 2008; Robitaille et al. 2008; Carey et al. 2009) have provided excellent road maps for studying these dense and cold clumps, especially the initial conditions for high-mass star formation (HMSF, Jiménez-Serra et al. 2010; Butler & Tan 2012; Peretto et al. 2013; Henshaw et al. 2016).

Corresponding author: Siyi Feng
siyi.s.feng@gmail.com

The column density ratio (relative abundance) between the deuterated and hydrogenated isotopologues of the same species, denoted $D(\text{hyd}) = \chi(\text{deu}/\text{hyd})$, is one of the most important chemical tools for diagnosing whether a particular core is in the prestellar or protostellar phase.

Formed at the birth of the Universe, deuterium (D) is slowly destroyed in the interiors of the stars, and mainly exists in molecular clouds in the form of HD (e.g., Millar et al. 1989; Ceccarelli et al. 2014). Atomic deuterium can be unlocked from the HD reservoir by the cosmic ray-driven ion-molecule chemistry at low temperature and high densities, starting from the isotopic exchange reactions with H_3^+ and leading to H_2D^+ , D_2H^+ , and D_3^+ (e.g., Caselli et al. 2002b; Crapsi et al. 2005; Vastel et al. 2006; Chen et al. 2010a). The deuterated ions can then donate deuterons to other species; this process is called deuterium fractionation.

The low-mass prestellar cores and high-mass cores in the earliest star-forming stage provide low-temperature and high column density environments, where gaseous heavy-element-bearing molecules such as CO start to freeze out onto the cold dust grains. As a result, the deuterium fractionations of several molecules are enhanced (Bacmann et al. 2003; Crapsi et al. 2005; Ceccarelli et al. 2007) toward these environments, showing higher D-fraction $D(\text{hyd})$ than the isotopic ratio $\mathcal{R}_{\text{D}/\text{H}}$ in the environment with little star formation (e.g., $\sim 10^{-5}$ in the diffuse interstellar medium (ISM), Oliveira et al. 2003; Linsky et al. 2006; Prodanović et al. 2010) by several orders of magnitude. After the young stellar object(s) are formed and warm the natal clouds up, molecules in the grain mantles especially CO, evaporate into the gas phase, destroying the deuterated isotopologues, so D-fraction of several species should decrease.

Comparing the D-fraction of various species between low-mass prestellar and protostellar objects (e.g., Crapsi et al. 2005; Emprechtinger et al. 2009), as well as between the high-mass clumps at the cold, young phase and more evolved phases (e.g., Pillai et al. 2006; Sakai et al. 2008; Chen et al. 2010a; Fontani et al. 2011; Miettinen et al. 2011; Vasyunina et al. 2011; Fontani et al. 2014; Gerner et al. 2015; Kong et al. 2015), previous observations found enhanced $D(\text{N}_2\text{H}^+)$ at low temperature, which is consistent with theoretical predictions (e.g., Caselli et al. 2002c; Albertsson et al. 2013). In contrast to the low-temperature enhancement of $D(\text{N}_2\text{H}^+)$, recent single-dish pointing observations (e.g., Fontani et al. 2015) show that, statistically, $D(\text{CH}_3\text{OH})$ is a good probe of the earliest protostellar phases, while $D(\text{NH}_3)$ does not show significant changes when the high-mass protostellar objects evolve. The deuterium fractionation efficiency seems species dependent, which may be due to their different gas-grain forming pathways.

The above conclusion is, however, not solid because of the limited number of species observed by previous works.

We also note that high-mass starless objects, which are used to compare with high-mass protostellar objects, may not be well classified. In fact, the evolutionary status of these sources classified by the traditional spectral energy distribution (SED) method is affected by large uncertainty due to the lack of continuum emission at IR wavelengths. Recent line observations at high angular resolution and high sensitivity have detected young stellar objects in candidates of “starless clumps”, invalidating the prestellar nature of these regions. For example, outflows have been detected toward young high-mass cores with bolometric luminosity-to-mass-ratios less than $1L_{\odot}/M_{\odot}$ (Feng et al. 2016c; Tan et al. 2016). More high-mass protostellar objects are detected toward $70\mu\text{m}$ dark clouds (e.g., Csengeri et al. 2017; Sanhueza et al. 2017), which have been called as “high-mass starless clump” candidates in previous works. These examples suggest that truly high-mass starless objects have a short lifetime or do not exist.

Therefore, conclusions from the previous observations of deuterated molecules may be affected by the wrong assumptions about the evolutionary phase of individual sources and unresolved star formation activities in single-dish pointing observations. A more accurate deuterium fractionation study requires the exploration of more species toward a sample of sources, for which we have well characterized their physical structures (i.e., the internal sources, the temperature profile, and the density profile) as well as knowledge of the dynamics (i.e., the star-forming activities and the evolutionary phases).

Targets: G28.34 P1 and S is a pair of high-mass clumps (H_2 column density 10^{24}cm^{-2}) located in the filamentary IRDC G28.34+0.06 (distance to the Galactic center $D_{\text{GC}} = 4.7\text{kpc}$, Wang 2018). Using the IRAM-30m, NOEMA, SMA, and ALMA, we have found that this pair of sources comprises different evolutionary stages (e.g., Wang et al. 2012; Feng et al. 2016c).

Clump S is located at the $70\mu\text{m}$ extinction peak of the filament. On a scale of 0.8pc , it shows low dust temperature ($14\text{--}16\text{K}$, Wang et al. 2008), low luminosity ($10L_{\odot}$, Ragan et al. 2013), and high CO depletion (Feng et al. 2016b), indicating that it is extremely young. However, on a scale of 0.08pc , we found extended bipolar red-shifted and blue-shifted lobes from SiO (2–1) and (5–4) emissions, indicating a young outflow (i.e., less energetic than the outflows from more evolved high-mass protostellar objects by a factor of at least 10, Feng et al. 2016c; Kong et al. 2018).

Clump P1 is an IR-bright source ($\sim 10^3L_{\odot}$, $18\text{--}28\text{K}$, Wang et al. 2011) located $1.5'$ northeast of S. Several intense CO outflows ($10^{-5}M_{\odot}\text{yr}^{-1}$, Wang et al. 2011; Zhang et al. 2015), water maser, and CH_3OH maser detections indicate that the young stellar objects embedded in P1 are more

evolved than those embedded in S (Wang et al. 2012; Wang 2015).

The P1 and S clump pair, showing evolutionary difference in the same molecular cloud, provides a good laboratory for studying the initial conditions of HMSF. In particular, by characterizing their dust and gas properties, we will be able to investigate the effects of environmental variations on the physio-chemical processes at different evolutionary phases.

In this paper, we present a detailed D-fraction study toward the G28.34 P1–S region incorporating data from IRAM-30 m observations. In Section 2 we summarize the observations and the data quality. We present the beam-averaged spectra toward P1 and S in Section 3.1 and show the maps of line spatial distributions in Section 3.2. We characterize the physical structures of P1 and S in Section 4, and present the D-fraction maps of six species in Section 5. In Section 6 we discuss the spatial correlation between the CO depletion and deuterium fractionation for different species. Finally, a summary of our main results can be found Section 7.

2. OBSERVATIONS

2.1. IRAM-30m

From 2014 May to 2017 September, we conducted an line imaging survey of our targets with the IRAM-30 m telescope at 1.3–4.3 mm. Observations were performed in the on-the-fly (OTF) mode, mapping two $1.5' \times 1.5'$ regions, centered at $18^{\text{h}}42^{\text{m}}50^{\text{s}}.740$, $-04^{\circ}03'15''.300$ (J2000) and $18^{\text{h}}42^{\text{m}}46^{\text{s}}.597$, $-04^{\circ}04'11''.930$ (J2000) for P1 and S, respectively. The broad bandpass of EMIR covers the 16 GHz bandwidth simultaneously for each spectral tuning. By superpositioning different spectral tunings, the frequency range covers 70.718–78.622, 82.249–101.981, 130.698–138.481, 151.818–175.481, and 217.019–224.800 GHz. Using the FTS200 backend, we achieve a frequency resolution of 0.195 MHz (corresponding to 0.637 km s^{-1} at 93.173 GHz). The angular resolution of the IRAM-30 m telescope is, for example, $\sim 11.9''$ at 218.760 GHz (Table 1). We had good weather conditions during the observations (the radiometer opacity τ at 255GHz is 0.16–0.38), and we used Saturn, 1749+096, or 1741-038 for pointing and focus. Using the corresponding forward efficiency (F_{eff}) and a main-beam efficiency (B_{eff}) at individual frequencies,¹ we converted the data from antenna temperature (T_{A}^*) to main-beam temperature ($T_{\text{mb}} = F_{\text{eff}}/B_{\text{eff}} \times T_{\text{A}}^*$). We used the GILDAS² software package for data reduction and line identification.³ The 1σ rms T_{mb} in the line free channels are 10.4–12.9 mK at 1.3–1.4 mm, 2.9–7.6 mK at 1.7–2.0 mm, 11.4–16.4 mK at

2.1–2.3 mm, 2.8–6.6 mK at 2.9–3.6 mm, and 3.1–3.6 mK at 3.8–4.3 mm.

2.2. Archival data

Furthermore, with the aim of characterizing the physical structure of the P1–S region, we use the following archival data:

The continuum data are obtained from *Herschel* Infrared Galactic Plane (Hi-GAL) survey at 70/160/250/500 μm (Molinari et al. 2010, obsID: 1342218694), from *CSO/SHARC-II* at 350 μm (PI: H. B. Liu), as well as from the combination of *Planck* and James Clerk Maxwell telescope (*JCMT*) - *SCUBA2* at 850 μm (Program ID: M11BEC30). The data quality is described in Lin et al. (2017).

The NH_3 (J, K)=(1,1) and (2,2) lines are observed with the Very Large Array (VLA; Wang et al. 2008) and Effelsberg-100 m single-dish telescope (Pillai et al. 2006). Continuum emission at 1.3 cm toward our source is not detected. After a combination in the UV-domain (Wang et al. 2008; Wang 2018), the data achieve an angular resolution of $\sim 5''$ and a velocity resolution of 0.6 km s^{-1} .

3. RESULTS

In this paper, we focus on the study of D-fraction by analyzing several pairs of hydrogenated and deuterated molecules that are detected in our IRAM-30 m line imaging survey.

A line is considered detected if its main-beam temperature is $> 4\sigma$. Table 1 lists all the detected lines in this paper. Their spectroscopic parameters are taken from the Cologne Database for Molecular Spectroscopy (CDMS,⁴ Müller et al. 2002, 2005) or from the Jet Propulsion Laboratory (JPL,⁵ Pickett et al. 1998).

3.1. Line profiles

Lines list in Table 1 in general have high critical densities ($> 10^4 \text{ cm}^{-3}$), high effective excitation density (Shirley 2015), and low E_u/k_{B} (except for some CH_3OH lines), and thus are dense and cold gas tracers. These lines are observed at different angular resolutions, allowing us to trace the gas properties of each clump on scales from 0.8 pc down to 0.2 pc.

To improve the signal-to-noise ratio (S/N) as well as to gauge the gas kinematics directly from the observations, we extract the beam-averaged spectra of each line from the 870 μm dust continuum peak P1 and S, without smoothing their native velocity or angular resolutions.

For HCO^+ , we note that the ^{12}C line is affected by self-absorption, as also found by Feng et al. (2016b). For HCN

¹ <http://www.iram.es/IRAMES/mainWiki/Iram30mEfficiencies>

² <http://www.iram.fr/IRAMFR/GILDAS>

³ The “Weeds” is an extension of GILDAS for line identification (Maret et al. 2011).

⁴ <https://cdms.astro.uni-koeln.de>

⁵ <http://spec.jpl.nasa.gov>

Table 1. Transitions Detected Toward G28.34 P1–S

Mol.	Freq. (GHz)	Transition	$S\mu^{2a}$ (D ²)	E_u/k_B^a (K)	n_{crit}^e ($\times 10^5 \text{ cm}^{-3}$)	n_{eff}^f ($\times 10^5 \text{ cm}^{-3}$)	Beam ($''$)
H ¹³ CN	86.340	J=1–0 ^c	26.7	4.1	9.3	2.2–3.5	30.0
H ¹³ CN	172.678	J=2–1 ^c	53.4	12.4	89.0	8.6–19.0	15.0
HC ¹⁵ N	86.055	1–0	8.9	4.1	9.8	--	30.1
DCN	72.415	J=1–0 ^c	26.8	3.5	5.5	--	35.8
HN ¹³ C	87.091	1–0	7.3	4.2	1.9	--	29.8
H ¹⁵ NC	88.866	1–0	7.3	4.3	2.0	--	29.2
DNC	76.306	1–0	9.3	3.7	1.7	--	34.0
H ¹³ CO ⁺	86.754	J=1–0 ^b	15.2	4.2	1.4	0.3–0.4	29.9
H ¹³ CO ⁺	173.507	J=2–1 ^b	30.4	12.5	28.4	1.0–1.7	15.0
HC ¹⁸ O ⁺	85.162	1–0	15.2	4.1	1.0	--	30.5
DCO ⁺	72.039	J=1–0 ^b	14.5	3.5	2.6	--	36.0
N ₂ H ⁺	93.173	J=1–0 ^c	104.0	4.5	1.5	0.1	27.8
N ₂ D ⁺	77.109	J=1–0 ^c	104.0	3.7	0.5	--	33.6
N ₂ D ⁺	154.217	J=2–1 ^c	208.1	11.1	9.2	--	16.8
NH ₃ ^d	23.694	1 ₁ 0a–1 ₁ 0s	6.6	23.8	0.1	0.01	
NH ₂ D	85.926	1 _{1,1} 0s–1 _{0,1} 0a	28.6	20.7	39.0	--	30.2
CH ₃ OH	76.510	5 _{0,5} –4 _{1,3} E	1.9	47.9	0.4	--	33.9
CH ₃ OH	84.521	5 _{–1,5} –4 _{0,4} E ^g	3.1	40.4	3.0	--	30.7
CH ₃ OH	95.169	8 _{0,8} –7 _{1,7} A ^g	7.2	83.5	1.6	--	27.3
CH ₃ OH	95.914	2 _{1,2} –1 _{1,1} A	1.2	21.4	0.5	--	27.0
CH ₃ OH	96.739	2 _{–1,2} –1 _{–1,1} E	1.2	12.5	82.5	--	26.8
CH ₃ OH	96.741	2 _{0,2} –1 _{0,1} A	1.6	7.0	0.5	--	26.8
CH ₃ OH	96.745	2 _{0,2} –1 _{0,1} E	1.6	20.1	3.4	--	26.8
CH ₃ OH	157.246	4 _{0,4} –4 _{–1,4} E	4.2	36.3	60.0	--	16.5
CH ₃ OH	157.271	1 _{0,1} –1 _{–1,1} E	1.5	15.4	1.8	--	16.5
CH ₃ OH	157.272	3 _{0,3} –3 _{–1,3} E	3.3	27.1	32.5	--	16.5
CH ₃ OH	157.276	2 _{0,2} –2 _{–1,2} E	2.4	20.1	1678.4	--	16.5
CH ₃ OH	170.061	3 _{2,1} –2 _{1,1} E	3.1	36.2	1963.1	--	15.3
CH ₃ OH	218.440	4 _{2,2} –3 _{1,2} E ^g	3.5	45.5	1.6	--	11.9
CH ₂ DOH	89.408	2 _{0,2} –1 _{0,1} e0	1.2	6.4	0.2	--	29.0
¹³ CH ₃ OH	94.405	2 _{–1,2} –1 _{–1,1} E	1.2	12.4	82.5	--	27.5
¹³ CH ₃ OH	94.407	2 _{0,2} –1 _{0,1} A	1.6	6.9	0.4	--	27.5
H ₂ CO	72.838	1 _{0,1} –0 _{0,0}	5.4	3.5	1.6	0.3–0.5	35.6
H ₂ CO	218.222	3 _{0,3} –2 _{0,2}	16.3	21.0	28.8	2.9–7.7	11.9
H ₂ CO	218.476	3 _{2,2} –2 _{2,1}	9.1	68.1	12.1	--	11.9
H ₂ CO	218.760	3 _{2,1} –2 _{2,0}	9.1	68.1	25.9	--	11.9

Note. ^a Line spectroscopic parameters are given according to catalogs including the JPL and CDMS;

^b Hyperfine splittings are recorded in JPL and CDMS but not resolved in our observations, so the sum of $S\mu^2$ is used for the rotational transitions to calculate the total column density;

^c Hyperfine splittings are resolved in our observations, and only the sum of $S\mu^2$ is needed for the rotational transitions to calculate the total column density;

^d Data are from the combination of VLA and Effelsberg, with a combined synthesized beam as $6.04'' \times 3.57''$ (position angle as -10.20°);

^e The critical density of each transition n_{crit} is derived from the Einstein coefficient A_{ij} and the collision rate C_{ij} at 5–20 K given by LAMDA (Schöier et al. 2005). We assume that the deuterated lines have the same C_{ij} as their hydrogenated counterparts;

^f The effective excitation density at kinetic temperature of 10–15 K from Shirley (2015), “--” labels the non-recorded value;

^g Known interstellar Class I methanol maser transitions (see Leurini et al. 2016, and the references therein).

and HNC, the main isotopologue ^{12}C line profiles show that multiple velocity components are present, as emission from various Galactic spiral arms is detected (Beuther & Sridharan 2007). Because we detect the ^{13}C , ^{18}O , or/and ^{15}N isotopologue lines of these species, we exclude the ^{12}C lines from discussion in this paper.

The spectra of key transitions detected from the hydrogenated-deuterated isotopologue pairs toward P1 and S are shown in Figure 1; the fits have been done by using the GILDAS package. All these transitions show a single velocity component at the given velocity resolution. If hyperfine splitting is resolved, we fit it by using the HyperFine-Structure (HFS) method, and derive the excitation temperature⁶ $T_{\Delta F}$ of the transition, if optically thick (Table 2, see Feng et al. 2016b for details). For the hyperfine splittings that are neither recorded in JPL/CDMS nor resolved in our observations, the line is fit by using the Gaussian (GAUSS) method. In the case that hyperfine splitting is recorded but is unresolved from our observations, we compare the fitting results by using the HFS and GAUSS methods, and find that broadening of the line width due to the hyperfine splitting is negligible. The best-fit parameters are listed in Table A1–A2.

In general, the molecular lines we study in this work show the same centroid velocities ($\sim 79.5 \text{ km s}^{-1}$) toward both P1 and S. Their line widths, in terms of the full width at half maximum (FWHM), are in the $3\text{--}5 \text{ km s}^{-1}$ range toward P1, and slightly ($< 20\%$) narrower toward S. In each clump, lines from different isotopologues of the same species have a similar FWHM, indicating that they trace the same bulk of gas. Specifically, when we compare the beam-averaged line profile of these molecules between S and P1, the hydrogenated molecular lines show stronger emission at their centroid velocities toward P1 than toward S by a factor of 1.5–2, which is consistent with the nature that P1 is chemically and physically more evolved. In contrast, the emission intensities at the centroid velocities of the deuterated molecular lines do not follow a unique enhancement trend from S to P1. The diversity of the measured D-fraction enrichment is discussed later in Section 3.2 and Section 5.5.

3.2. Line spatial distribution maps

To compare the spatial distribution of deuterated and hydrogenated molecules, the line intensities are integrated over the same velocity range (listed in Table A1),⁷ and they are shown as color maps in Figure 2. To compare the spatial correlation between the dust and gas distribution, the contin-

uum emission is overlaid as white contours on each of the line maps. Because P1 and S are dark at wavelengths shorter than $70 \mu\text{m}$ (Feng et al. 2016a), we chose the $870 \mu\text{m}$ APEX continuum emission (Schuller et al. 2009) as representative of the dust distribution.

In clump P1, all the lines of hydrogenated molecules show their emissions at a local maximum position coincident with the $870 \mu\text{m}$ continuum peak, while in clump S, these molecules show emission at a local maximum position $\sim 20''$ northeast (NE) to the $870 \mu\text{m}$ continuum peak.

The deuterated molecules present their strongest emissions at different locations within the P1–S region: (1) Most lines, for example N_2D^+ (1–0), DNC (1–0), and NH_2D ($1_{1,1}0_{\text{s}}\text{--}1_{0,1}0_{\text{a}}$), show the strongest emission at $\sim 20''$ offset NE of clump S, where ^{13}CO , C^{18}O , and C^{17}O show high depletion (Feng et al. 2016b, also see Section 6); (2) DCN (1–0) shows the strongest emission toward P1; (3) Although we are not able to confirm the location where CH_2DOH ($2_{0,2}\text{--}1_{0,1}$) shows the strongest emission due to $\text{S/N} < 4$ in most pixels, the emission maximum appears at $\sim 25''$ offset NE of clump S.

We note that an offset of $20''$ corresponds to $2/3$ of the beam at 3 mm . Because these lines are observed simultaneously, the different locations of their individual emission maxima is likely the result of their different distributions, rather than any uncertainty caused by the pointing error between the IRAM-30 m (for molecular lines) and APEX (for the dust continuum) telescopes. Hereafter, we denote this location ($20''$ NE of S) as “Soff”.

4. PHYSICAL STRUCTURE

We have detected deuterated isotopologues of six species: HCN, HNC, HCO^+ , N_2H^+ , NH_3 , and CH_3OH . They are believed to have different gas-grain formation routes (e.g., Fontani et al. 2015). To understand how different environments affect the deuterium fractionation process, it is essential to characterize the physical structure of the source, i.e., via reconstructing the gas and dust temperature as well as density profiles.

4.1. Dust temperature and density maps

Following the iterative SED fitting procedure described in Lin et al. (2017), we establish a reliable blackbody model and obtain the dust opacity index β map at an angular resolution of $22''$ using the archival *Herschel* PACS 70, 160, *Herschel* SPIRE 250 maps, the $350 \mu\text{m}$ map by combining *Herschel* SPIRE and CSO/SHARC-II, as well as the $850 \mu\text{m}$ map by combining the deconvolved Planck 353 GHz and JCMT-SCUBA2 data (Section 2.2). Then, assuming the β map has no local variation from $22''$ to $10''$ resolution, we apply the Monte Carlo method to fit the continuum data from *Herschel* PACS at $70 \mu\text{m}$ and from CSO/SHARC-II at $350 \mu\text{m}$. At an

⁶ We use a subscript to specify the excitation temperature derived from different J levels ($T_{\Delta J}$), (J, K) levels ($T_{\Delta J, \Delta K}$), and F levels ($T_{\Delta F}$, $T_{\Delta F1, \Delta F}$).

⁷ In the case that a particular line shows resolved hyperfine splittings, we integrate its intensity over the entire velocity range, which covers all the hyperfine components.

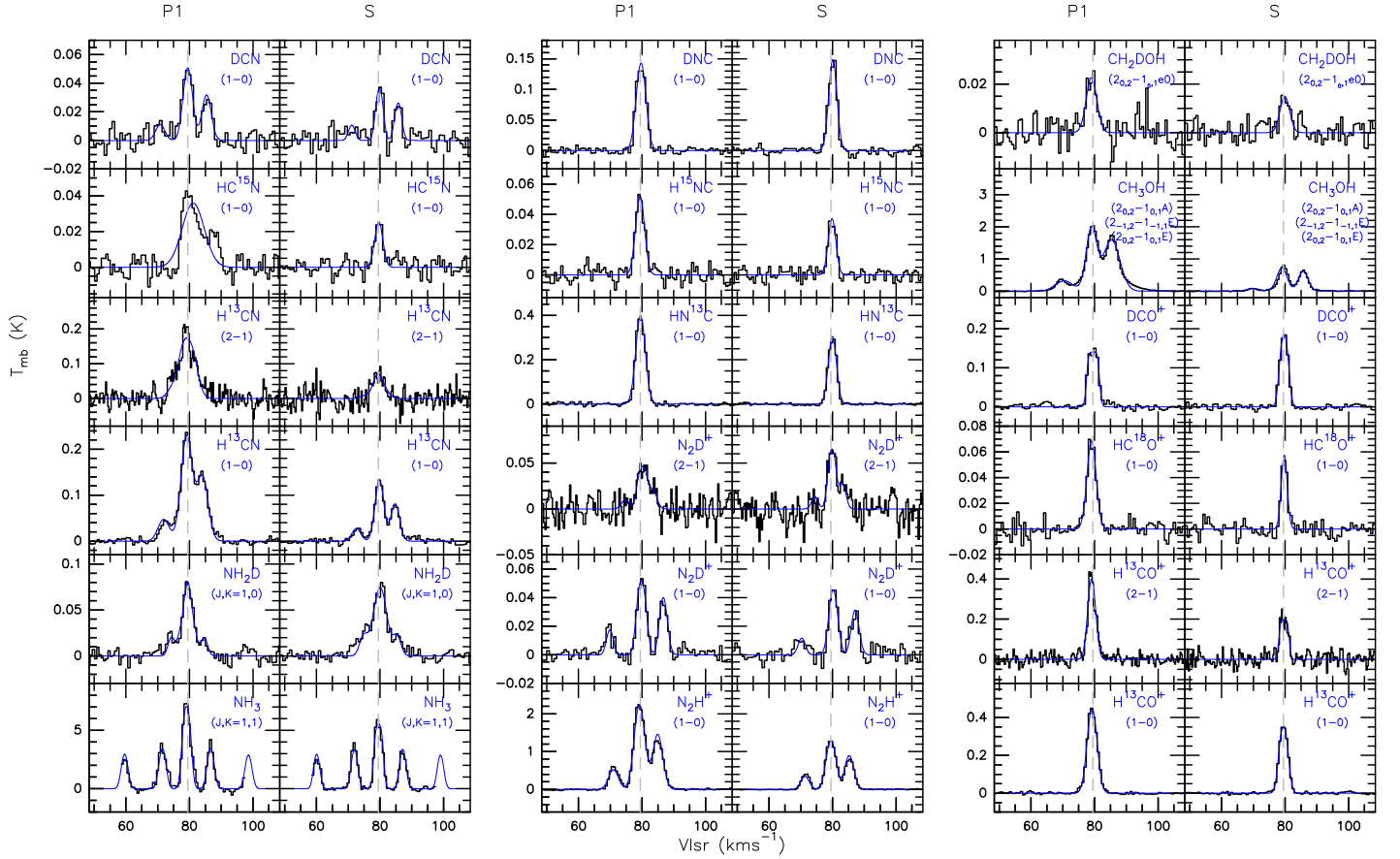


Figure 1. Beam-averaged spectra of identified lines from deuterated-hydrogenated isotopologue pairs extracted from P1 and S. The positions are labeled at the top of each column. All lines are extracted from images that we regridded to the same pixel size, but whose native angular and velocity resolution we kept as in the observations (see beam information in Table 1). The best-fit parameters by using the GAUSS or HFS methods are listed in Table A1 and Table A2, and the synthetic spectrum for each line is plotted in blue. The system velocity (79.5 km s^{-1}) is shown as a gray dashed line in each panel.

angular resolution of $10''$, we obtain the maps of H_2 column density $N(\text{H}_2)$ and dust temperature $T(\text{dust})$ simultaneously toward P1–S. The detailed fitting procedure is also given in Appendix A.

As shown in Figure 3I and 3III, P1 and S cannot be modeled as spherical sources at a linear resolution of 0.2 pc ; instead, they show 2D Gaussian structures in the plane of the sky. Therefore, instead of extracting the temperature and column density profiles averaged along the radii of each clump, hereafter we extract the physical and chemical parameters along three directions in the plane of the sky: (1) the filamentary elongation along P1 and S, (2) perpendicular to the filament elongation with the center on $870 \mu\text{m}$ continuum peak P1, and (3) perpendicular to the filament elongation with the center on $870 \mu\text{m}$ continuum peak S. Given that the separation between P1 and S is only $\sim 80''$ (1.8 pc) in the plane of the sky, the gas and dust properties along the P1–S ridge of the filament may be influenced by both clumps, while those in the perpendicular direction and centered on a particular clump are likely less impacted by the distant clump. To vi-

ualize the mutual effects of clumps P1 and S on each other, we set the starting and end point of each direction (points labeled as “a”, “b”, “c”, “d”, “e”, “f”) as an offset of $\pm 40''$ to the center P1 or S.

Inspecting Figure 3, we note a larger uncertainty of the H_2 column density and dust temperature toward S than toward P1. This is a compromise made to obtain the maps at a higher angular resolution by including the *Herschel* $70 \mu\text{m}$ data in the SED fits. Nevertheless, our fits indicate that the P1–S region is dense⁸ ($\sim 10^5 \text{ cm}^{-3}$) and cold ($\sim 19 \text{ K}$), with the H_2 column density ($\sim 1.2 \times 10^{23} \text{ cm}^{-2}$) toward P1 higher than that toward S by a factor of 2.

We also note a decrease ($\sim 4 \text{ K}$) of the dust temperature from the outskirts of the filament to the center. Because the dust temperature derived from SED fitting traces the weighted average temperature along the line of sight (e.g.,

⁸ The average volume number density n of the gas can be estimated from the source kinematic distance D_{GC} , the angular resolution θ , and the H_2 column density $N(\text{H}_2)$ as $n = \frac{N(\text{H}_2)}{\theta D_{GC}}$.

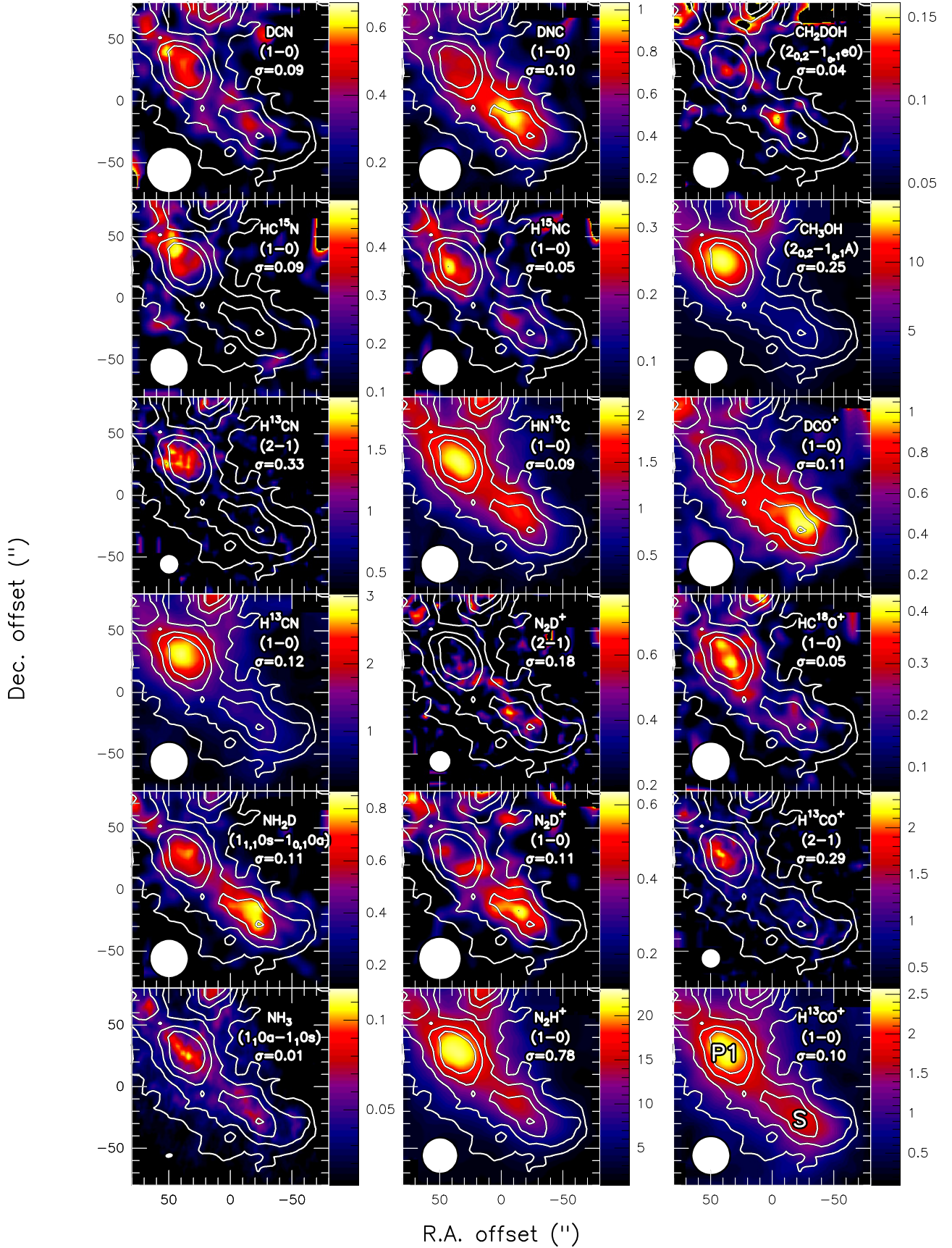


Figure 2. Molecular line distributions shown as color maps. The line intensities are integrated over their entire velocity dispersion (listed in Table A1) and shown in units of main-beam temperature as K km s⁻¹. The transition of each line and 1σ rms (K km s⁻¹) of each image are given, with the angular resolution shown as a beam in white in the bottom left corner of each panel. The white contours show the continuum emission from 870 μ m APEX data at an angular resolution of 18.2'' (Schuller et al. 2009), starting from 5σ and increasing by 5σ ($\sigma = 0.042$ Jy beam⁻¹). The P1 and S denominations are shown in the bottom right panel.

Sokolov et al. 2018), such a decrease can be explained considering that the heating from the protostellar objects P1 and S to their gas envelopes is comparably less efficient than the interstellar radiation impinging on the outskirts of this filament.

4.2. Gas temperature and density maps derived from p -NH₃

The dust continuum map suffers from the contamination of the foreground and background dust. In contrast to this, we can integrate the line intensity of a gaseous species over its velocity dispersion around the system velocity of the target source, so that the gas emission map toward the source can be well characterized by excluding the foreground/background contamination (Section 3.1).

CO isotopologues are relatively more abundant than the other species. Our observations imaged C¹⁸O(2–1) and C¹⁷O(2–1) lines with high S/N. They show similar line profiles to the lines we study in this work (see Feng et al. 2016b). Although 2–1 transitions of CO isotopologues are easily thermalized near their critical densities ($2 \times 10^4 \text{ cm}^{-3}$ at 10–20 K, derived using data from the Leiden Atomic and Molecular Database, LAMDA⁹), CO is known to freeze out at an environment of $T < 20 \text{ K}$ and density slightly higher than a few 10^4 cm^{-3} (e.g., Caselli et al. 1999; Fontani et al. 2006; Aikawa et al. 2008). Therefore, showing high depletion (Feng et al. 2016b, see also Section 6), it cannot be used as a high-density tracer.

Compared with CO, N-bearing species are more resilient to depletion (e.g., Caselli et al. 1999; Bergin et al. 2002; Caselli et al. 2002a; Jørgensen et al. 2004). The (1,1) and (2,2) inversion transition lines of NH₃, with their critical density of $(1-2) \times 10^3 \text{ cm}^{-3}$ (Shirley 2015) in the temperature range of 20–100 K, provide a sensitive gas thermometer in the cold environment (e.g., Ho & Townes 1983; Walmsley & Ungerechts 1983; Crapsi et al. 2007; Rosolowsky et al. 2008; Juvela & Ysard 2011). Given that the dipole transitions between its different K ladders are forbidden, the ortho ($K = 3n$) and para ($K \neq 3n$) spin states of NH₃ behave as distinct species. An accurate gas kinetic temperature should be derived from either para (p) or ortho (o) lines (e.g., Ragan et al. 2011; Battersby et al. 2014; Wang et al. 2014; Bihl et al. 2015; Svoboda et al. 2016).

At an angular resolution of $\sim 5''$ and a velocity resolution of 0.6 km s^{-1} , the NH₃ (J, K)=(1,1) and (2,2) lines obtained from the combination of the VLA and Effelsberg-100 m show one velocity component in the P1–S region. Applying the Monte Carlo fitting tool HfS developed by Estalella (2017) to our VLA-Effelsberg combined data,¹⁰ we derive the value

Table 2. Excitation temperature derived from hyperfine transitions or from line ratios

Line	T	P1 (K)	Soff (K)	S (K)
p -NH ₃ (1,1)	$T_{(\Delta F_1, \Delta F)}$	20.0 ± 10.1	10.4 ± 13.2	10.2 ± 1.0
p -NH ₃ (2,2)/(1,1)	$T_{(\Delta J, \Delta K)}$	18.0 ± 2.6	13.5 ± 2.9	14.0 ± 3.9
o -NH ₂ D(1,0)	$T_{\Delta F}$	3.0 ± 2.4	5.7 ± 2.9	3.0 ± 2.4
N ₂ H ⁺ (1-0)	$T_{\Delta F}$	8.1 ± 5.1	6.0 ± 2.8	5.2 ± 2.4
N ₂ D ⁺ (2-1)/(1-0)	$T_{\Delta J}$	4.5 ± 1.2	4.0 ± 0.5	3.8 ± 0.5
H ¹³ CN(1-0)	$T_{\Delta F}$	8.7 ± 6.9	9.5 ± 7.4	8.6 ± 5.2
H ¹³ CN(2-1)	$T_{\Delta F}$	3.5 ± 2.8	8.2 ± 5.6	— ^a
DCN(1-0)	$T_{\Delta F}$	4.2 ± 3.3	3.2 ± 1.8	3.5 ± 1.5
H ¹³ CN(2-1)/(1-0)	$T_{\Delta J}$	3.8 ± 0.5	3.2 ± 1.7	3.0 ± 0.3
H ¹³ CO ⁺ (2-1)/(1-0)	$T_{\Delta J}$	4.1 ± 0.3	3.6 ± 0.3	— ^a

Note. ^a S/N < 4

and uncertainty maps for the following parameters: (1) the excitation temperature $T_{(\Delta F_1, \Delta F)}$ for the (1,1) hyperfine splitting, derived from the main and satellite lines with different quantum numbers ($\Delta \vec{F}_1, \Delta \vec{F}$); (2) the rotation temperature $T_{(\Delta J, \Delta K)}$, derived from the (1,1) and (2,2) inversion states, which are not radiatively coupled; (3) the kinetic temperature T_{kin} (Figure 4I), based on the Maret et al. (2009) approximation, by taking the collision transitions into account; (4) the total column density $N(\text{NH}_3)$ (Figure 4III), derived from the (1,1) and (2,2) inversion states, with an assumption of ortho-to-para ratio (OPR) of 1.

We found that $T_{(\Delta F_1, \Delta F)}$ derived from (1,1) hyperfine splitting lines is close to the rotation temperature $T_{(\Delta J, \Delta K)}$ (Table 2) and the gas kinetic temperature T_{kin} at each pixel, the 3–5 K difference between them is within the systematic uncertainty given by the Monte Carlo approach. Therefore, we can reasonably assume that p -NH₃ lines are thermalized and under local thermodynamic equilibrium (LTE) conditions, and hence the constant excitation temperature approximation (the CTEX method, Caselli et al. 2002b) is valid for the multilevel system of NH₃ (J, K) = (1, 1) in our target region.

On the one hand, we find that the gas kinetic temperature derived from p -NH₃ (Figure 4II) has a larger dynamic range than the dust temperature ($\sim 19 \text{ K}$, Figure 3II) along the filament elongation (see also in Wang 2018), with P1 ($20 \pm 3 \text{ K}$) slightly warmer than S ($14 \pm 3 \text{ K}$). On the other hand, NH₃ shows the column density maximum toward “Soff” ($\sim 10^{16} \text{ cm}^{-2}$), higher than that toward S and P1 by a factor of 2 and 3, respectively (Figure 4IV), which is opposite to the trend found with the dust column density (Figure 3IV). Therefore, gas temperature and volume density may play an important role for the gas chemistry variations along the fil-

⁹ <http://home.strw.leidenuniv.nl/~moldata>

¹⁰ We compare the fitting results to our NH₃ (2,2)/(1,1) data by using HfS, CLASS/GILDAS, and PySpecKit (Ginsburg & Mirocha 2011). Although

the values of the fitting parameters from these softwares agree with each other, CLASS and PySpecKit seem to underestimate the uncertainty of the parameters (Estalella 2017).

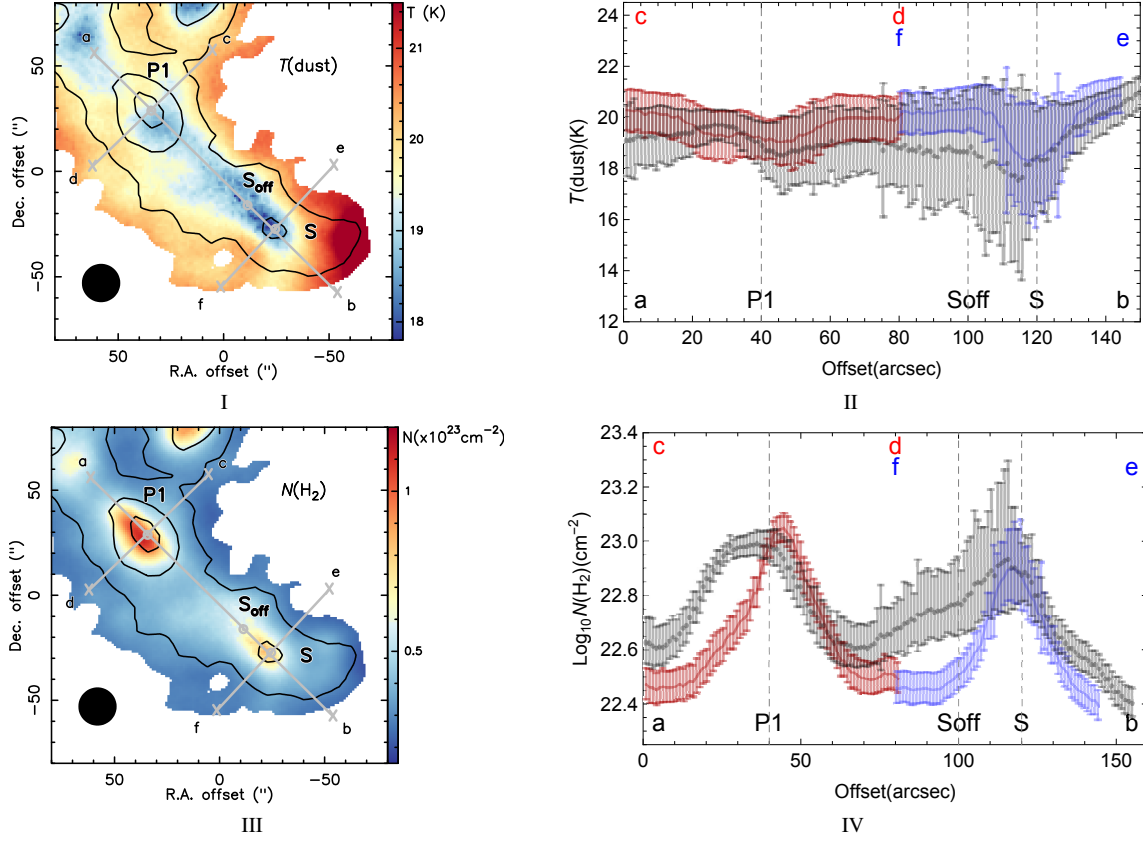


Figure 3. Dust temperature and H₂ column density maps for G28.34 P1–S. Maps are derived by iterative SED fits to the data from *Herschel* PACS at 70 μm and from *CSO/SHARC-II* at 350 μm , achieving an angular resolution of 10'' (Lin et al. 2017). The continuum images at 70, 160, 250, 350, 500, and 850 μm from *Herschel*, *CSO/SHARC-II*, *Planck*, and *JCMT-SCUBA2* are used to establish a reliable blackbody model pixel by pixel. *Panel I*: dust temperature map. *Panel II*: dust temperature profile extracted along the the filamentary elongation, plotted in black, with the ends labeled as “a” and “b”; dust temperature profiles extracted along the perpendicular direction to the filamentary elongation is plotted in red (from point “c” over the 870 μm continuum peak P1 to point “d”) or blue (from point “e” over the 870 μm continuum peak S to point “f”). *Panel III*: H₂ column density map. *Panel IV*: H₂ column density profile in the directions of a–b (in black), c–d (in red), and e–f (in blue). The pixels with $< 5\sigma$ continuum emission at 870 μm are blanked. The black contour of the 870 μm continuum emission starts from 10σ and increases in steps of 10σ ($\sigma = 0.042 \text{ Jy beam}^{-1}$). The angular resolution achieved in SED fits is shown in black in the bottom left corner of *Panels I, III*.

ament, from P1 to S.

4.3. Gas temperature from p -H₂CO and CH₃OH

Taking advantage of the broad bandwidth of our IRAM-30 m observations, we detected four p -H₂CO lines, three A-type CH₃OH lines and eleven E-type CH₃OH lines, with different (J , K) levels and E_u/k_B spanning the range of 7–84 K (Table 1). Both species are likely formed on the surface of dust grains by successive hydrogenation of CO (Watanabe & Kouchi 2002; Woon 2002; Hidaka et al. 2004), and are believed to be precursors of large complex organic molecules (Barone et al. 2015). In addition to NH₃, both species are usually taken as typical thermometers (e.g., Mangum & Wootten 1993; Caselli et al. 1993; Johnstone et al. 2003; Leurini et al. 2004, 2007; Giannetti et al. 2017). Using different (J , K) level lines with higher critical density and effective excitation density than NH₃ (1,1) and (2,2), we can trace the temperature of denser gas (e.g., Ao et al. 2013; Ginsburg et al. 2016; Tang et al. 2018).

For each species, we assume that all lines are optically thin and under LTE. After smoothing all lines to the same angular resolution (Figure A1 and A2), we use the rotational diagram (RD) method (see, e.g., Feng et al. 2015) to derive the rotation temperature (T_{rot}) map as well as the molecular total column density (N_{rot}) map for a particular species. Although A-type and E-type CH₃OH cannot be interconverted in chemical reactions, the partition functions of both types are the same (Rabli & Flower 2010). Therefore, we do not separate them in the RD calculation. T_{rot} of p -H₂CO and CH₃OH extracted from P1, S, and Soff in Table 3 are consistent with T_{kin} derived from p -NH₃ (Figure 4).

Furthermore, we note that lines at 1 mm, 2 mm, and 3 mm with different E_u/k_B may in fact trace gas from different layers of the source envelope. Given that some low- J lines might be optically thick, and the lines with high critical densities ($> 10^6 \text{ cm}^{-3}$) might be in non-LTE, we use the large velocity gradient (LVG) approximation to fit the p -H₂CO, A-CH₃OH, and E-CH₃OH lines individually.

Using the statistical equilibrium radiative transfer code RADEX (van der Tak et al. 2007) and a related solver (Fujun Du’s myRadex¹¹) as well as the MultiNest algorithm (Feroz & Hobson 2008; Feroz et al. 2009, 2013), we derive the probability density function (PDF) of parameters, including the H₂ number density n , molecular column density N_{col} , the gas kinetic temperature T_{kin} , and the filling factor, toward P1, S, and Soff (see Figure A3 as an example).

When we assume that all lines from the same species have the same filling factors, our results show that the filling factors are close to unity for both species. While A-/E-CH₃OH

seem to trace a denser region ($> 10^5 \text{ cm}^{-3}$) compared to p -H₂CO ($\sim 5 \times 10^4 \text{ cm}^{-3}$), T_{kin} from these tracers is consistent, showing a decrease from P1 (28–50 K) to Soff (16–24 K) and S (19–26 K).

We note that T_{kin} measured from A-/E-CH₃OH and p -H₂CO at P1, S, and Soff are in general higher than their T_{rot} . One possible reason for this is that these CH₃OH and H₂CO lines are subthermally excited in our sources (e.g., Kalenskii & Kurtz 2016). Moreover, in P1 and S shock environment, some CH₃OH lines may be masering (e.g., at 84.521, 95.169, and 218.440 GHz in Table 1), and this phenomenon cannot be solved by RADEX (van der Tak et al. 2007). Furthermore, n , N_{col} , and T_{kin} are three free parameters in our LVG fit, and the best-fit result has an intrinsic degeneracy in the parameter combination. Therefore, we are not able to tell the precise value of individual parameters from the multiparameter fits.

Nevertheless, the molecular column densities toward individual positions from LVG are consistent with the estimation under LTE assumption, showing an increase from S and Soff to P1 by a factor of 3–5. Therefore, we believe that the LTE-RD analysis provides a good approximation to LVG, in obtaining the gas temperature and molecular column density maps of H₂CO and CH₃OH.

5. MOLECULAR DEUTERIUM FRACTION MAPS

The environmental differences along the filament from P1 to S are small but not negligible. To quantify the effects of environmental changes on the deuterium fractionation of different species, molecular column densities need to be measured precisely.

According to Figure 1, isotopologue lines with the same J -level from the same species have the same E_u/k_B , and they show similar line profiles toward the same source. Therefore, after smoothing them to the same angular resolution, we assume that they trace the same gas, and that the excitation effect is excluded for any variations at different pixels. Moreover, most lines show extended emission in the plane of the sky, so we assume that they do not suffer from beam dilution.

Note that most rotational transitions in our study show resolvable hyperfine splittings. Previous studies simplified the estimation of the total molecular column density of one species, based on an assumption that all of its transitions have a constant excitation temperature (i.e., “CTEX” approximation). Unlike the NH₃ (1,1) line which is in LTE toward the P1–S region (Section 4.2), this method may not tell the precise column densities of the dense gas tracers if they are in non-LTE. For example, low- J lines of HCO⁺, HCN, and N₂H⁺ isotopologues are not sensitive to the excitation temperature changes between 5 and 10 K (see the discussion in Shirley et al. 2013 and Mangum & Shirley 2015). Therefore, when the measured excitation temperature falls into this

¹¹ See <https://github.com/fjdu/myRadex>.

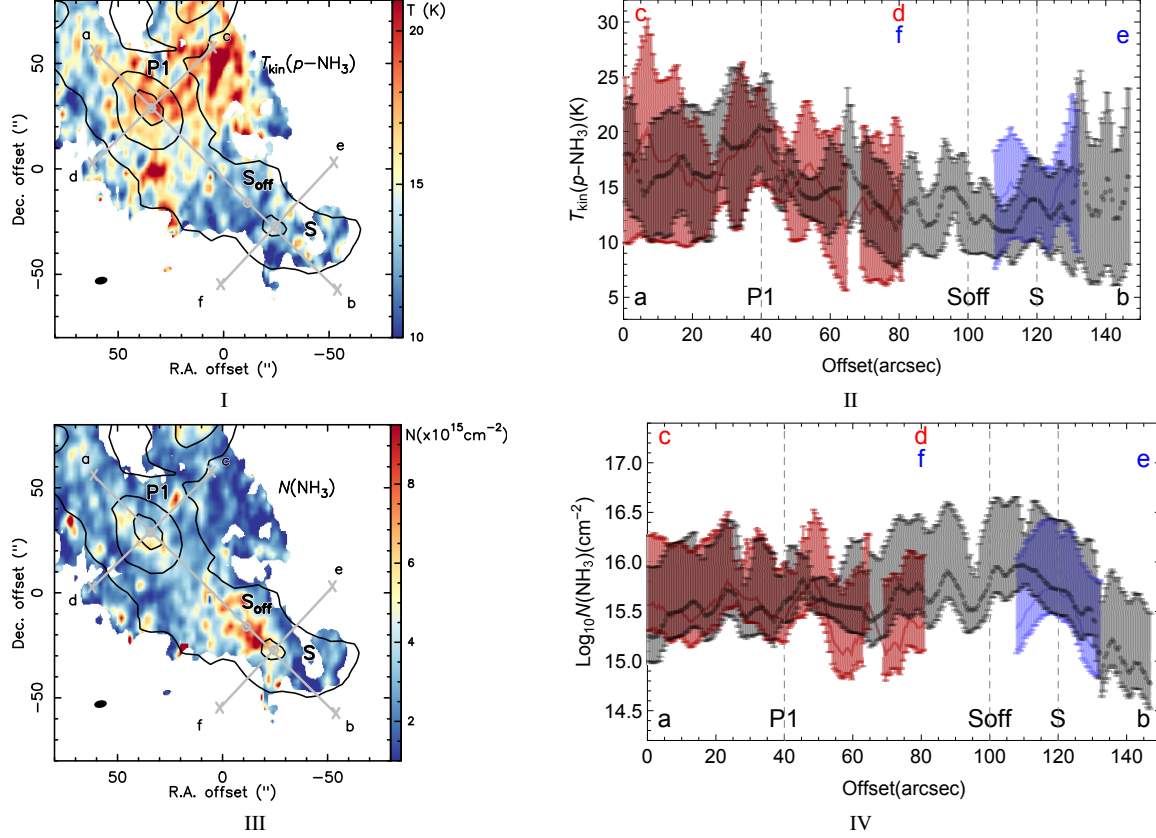


Figure 4. Gas kinetic temperatures and NH_3 column densities derived from the multilevel system of $p\text{-NH}_3$. *Panel I:* the gas kinetic temperature T_{kin} map. *Panel II:* the gas kinetic temperature profiles in the directions of a–b (in black), c–d (in red), and e–f (in blue); *Panel III:* the NH_3 column density map with assumptions of no beam dilution and an OPR of 1; *Panel IV:* the NH_3 column density profiles in the directions of a–b (in black), c–d (in red), and e–f (in blue). The black contour of $870 \mu\text{m}$ continuum emission starts from 10σ and increases in steps of 10σ ($\sigma = 0.042 \text{ Jy beam}^{-1}$). The labeled positions are the same as those in Figure 3. The pixels where the NH_3 (J, K) = (1, 1) line shows $< 4\sigma$ integrated intensity are blanked in each panel. The synthesized beam of the VLA-Effelsberg combined data is shown in the lower left corner of *Panel I, III*.

Table 3. Mean and standard deviation of parameters from LVG and LTE RD fittings

Mol.	Position	LVG			LTE	
		n (10^5 cm^{-3})	T_{kin} (K)	N_{col} (10^{14} cm^{-2})	T_{rot} (K)	N_{rot} (10^{14} cm^{-2})
$p\text{-H}_2\text{CO}$	P1	0.5 ± 0.1	51.6 ± 6.2	0.3 ± 0.0	19.3 ± 6.5	0.8 ± 0.7
$p\text{-H}_2\text{CO}$	S	0.5 ± 0.1	26.4 ± 2.0	0.1 ± 0.0	14.3 ± 3.6	0.2 ± 0.1
$p\text{-H}_2\text{CO}$	Soff	0.5 ± 0.2	19.5 ± 1.5	0.1 ± 0.0	13.0 ± 2.9	0.2 ± 0.1
A- CH_3OH	P1	4.8 ± 0.9	28.1 ± 1.3	4.9 ± 0.4	23.4 ± 7.8	2.9 ± 2.1
E- CH_3OH	P1	2.1 ± 0.1	40.6 ± 2.8	2.8 ± 0.1		
A- CH_3OH	S	5.1 ± 0.8	22.4 ± 0.8	1.1 ± 0.1	20.1 ± 5.8	0.8 ± 0.5
E- CH_3OH	S	1.3 ± 0.5	19.3 ± 1.5	0.9 ± 0.1		
A- CH_3OH	Soff	2.9 ± 0.4	24.2 ± 1.2	1.0 ± 0.1	19.2 ± 0.5	0.7 ± 0.5
E- CH_3OH	Soff	1.2 ± 0.0	16.0 ± 1.1	0.9 ± 0.1		

range, it might be only a lower limit of the real excitation temperature.

For the following species, we measure the excitation temperatures of the detected transitions, and compare their measured D-fractions by using CTEX method with those measured by using T_{kin} .

5.1. NH_2D Column Density and Deuterium Fraction of NH_3

Our observations only cover one *o*- NH_2D (J, K)=(1,0) line, with hyperfine splitting marginally resolved at a velocity resolution of 0.7 km s^{-1} . This line has a high critical density ($4 \times 10^6 \text{ cm}^{-3}$ at 5–20 K), so it might not be thermalized in our sources. Moreover, HFS fitting indicates that the main line of this transition is optically thin toward P1 ($\tau \sim 0.4$) and S ($\tau \sim 0.9$). For a single transition, the observed brightness temperature is a function of $T_{\Delta F}$, the unknown filling factor, and the line optical depth. Therefore, the $T_{\Delta F}$ derived from fitting the line profile of a single transition ($< 6 \text{ K}$ with large uncertainty, Table 2) may be underestimated.

A plausible column density map of NH_2D can be given using T_{kin} from NH_3 fitting. Here, we assume the OPR of NH_2D and NH_3 as statistical values of 3 and 1, respectively (e.g., Fontani et al. 2015; Harju et al. 2017), and derive the D-fraction from NH_3 to NH_2D by converting the column densities of *o*- NH_2D and *p*- NH_3 into total (*o+p*) column densities.

The single D-fraction of NH_3 , shown as $\chi(\text{NH}_2\text{D}/\text{NH}_3)$ in Figure 5, seems to be almost uniform, as $(5 \pm 3) \times 10^{-3}$ in the entire P1–S region, indicating small sensitivity to the gas temperature variation when $T_{\text{kin}} < 22 \text{ K}$.

5.2. Deuterium Fraction of N_2H^+ , HCN, HCO^+ , and HNC

The low- J transitions of N_2H^+ , HCN, HCO^+ , and HNC isotopologues are typical dense gas tracers (with critical densities of 10^5 – 10^6 cm^{-3}). In this work, we derive the column densities of the hydrogenated molecules by assuming that N_2H^+ (1–0) and the lines from ^{13}C isotopologues are optically thin at pixels where $S/N > 4$ for the following reasons: (1) The main hyperfine line of N_2H^+ (1–0) has a small optical depth toward P1 and S ($\tau=0.1$ – 0.3). (2) The 1–0 lines of ^{13}C isotopologues show a homogeneous intensity ratio with respect to their less abundant isotopologue lines HC^{15}N (1–0), H^{15}NC (1–0), and HC^{18}O^+ (1–0) in the entire P1–S region (see the discussion in Section 5.4). (3) Compared with the ^{15}N or ^{18}O lines, the ^{13}C lines show a higher S/N toward each pixel.

The hyperfine splittings of N_2H^+ (1–0), H^{13}CN (1–0), H^{13}CN (2–1), and DCN (1–0) are marginally resolved at our velocity resolution, and blended into three Gaussian peaks (Fig. 1). For these, we derive the excitation temperature ($T_{\Delta F}$) for each single line using the HFS method. Moreover, we detected two low- J transitions (2–1 and 1–0) of N_2D^+ and H^{13}CN , so the excitation temperatures ($T_{\Delta J}$) of both isotopologues can be derived using lines at different J levels.

Listing $T_{\Delta F}$ and $T_{\Delta J}$ in Table 2, we find they are comparable for all species, implying that the CTEX method is a good approximation to estimate the column density of these molecules.

Note that the detected lines are all low- J transitions, with E_u/k_B spanning the range of 4–12 K. Therefore, like the case of NH_2D (J, K)=(1,0), the excitation temperatures that fall in the range of 3–10 K may be underestimated.

We estimate the column densities of individual molecules using the maps of $T_{\Delta J}$ (as a lower limit) and T_{kin} derived from *p*- NH_3 , separately. For HN^{13}C , there is only one line detected in this work, so the $T_{\Delta J}$ we use as approximation is derived from H^{13}CN lines. The molecular column densities derived from two sets of temperature maps are similar within the systematic uncertainty.

Furthermore, using the isotopic ratio $\mathcal{R}_{^{12}\text{C}/^{13}\text{C}} = 7.5D_{GC} + 7.6 = 42.9$ (Giannetti et al. 2014), we convert the column density map of the ^{13}C isotopologues to those of the ^{12}C isotopologues, and show the D-fraction maps in Figure 5. Although the T_{kin} map shows a larger dynamic range than the $T_{\Delta J}$ maps, the D-fraction maps derived from both sets of temperatures show the same enhancement from P1 to S by a factor of 2–3.

5.3. Deuterium Fraction of CH_3OH

Because the LTE and non-LTE analysis give similar CH_3OH column density values toward P1, S, and Soff, and the T_{rot} map of CH_3OH agrees with the T_{kin} map derived from *p*- NH_3 (Section 4.3), we estimate the CH_2DOH column density by assuming that its only detected line is optically thin, and that the T_{rot} map derived from the CH_3OH lines can be applied to CH_2DOH . The map of CH_2DOH relative abundance ratio with respect to CH_3OH , shown as $\chi(\text{CH}_2\text{DOH}/\text{CH}_3\text{OH})$ in Figure 5, indicates an enhancement peak at Soff.

5.4. Error budget

During our observations with the EMIR receiver, the uncertainty in the absolute flux calibration^{12, 13} was $< 10\%$ (Carter et al. 2012). Comparing different line-fitting methods, we found that the uncertainty in the integrated intensity measurement is $< 30\%$, as the result of the line blending at the given velocity resolution, as well as the velocity range we select to integrate the lines (Table A1). In calculating the molecular column densities and relative abundance ratios, uncertainties are given by following the error propagation formulae.¹⁴ More importantly, the following assump-

¹² See <http://www.iram.fr/GENERAL/calls/s17/30mCapabilities.pdf>

¹³ See also *Calibration of spectral line data at the IRAM 30m radio telescope* by C. Kramer (1997).

¹⁴ See calculations in <https://bit.ly/2J92r10>

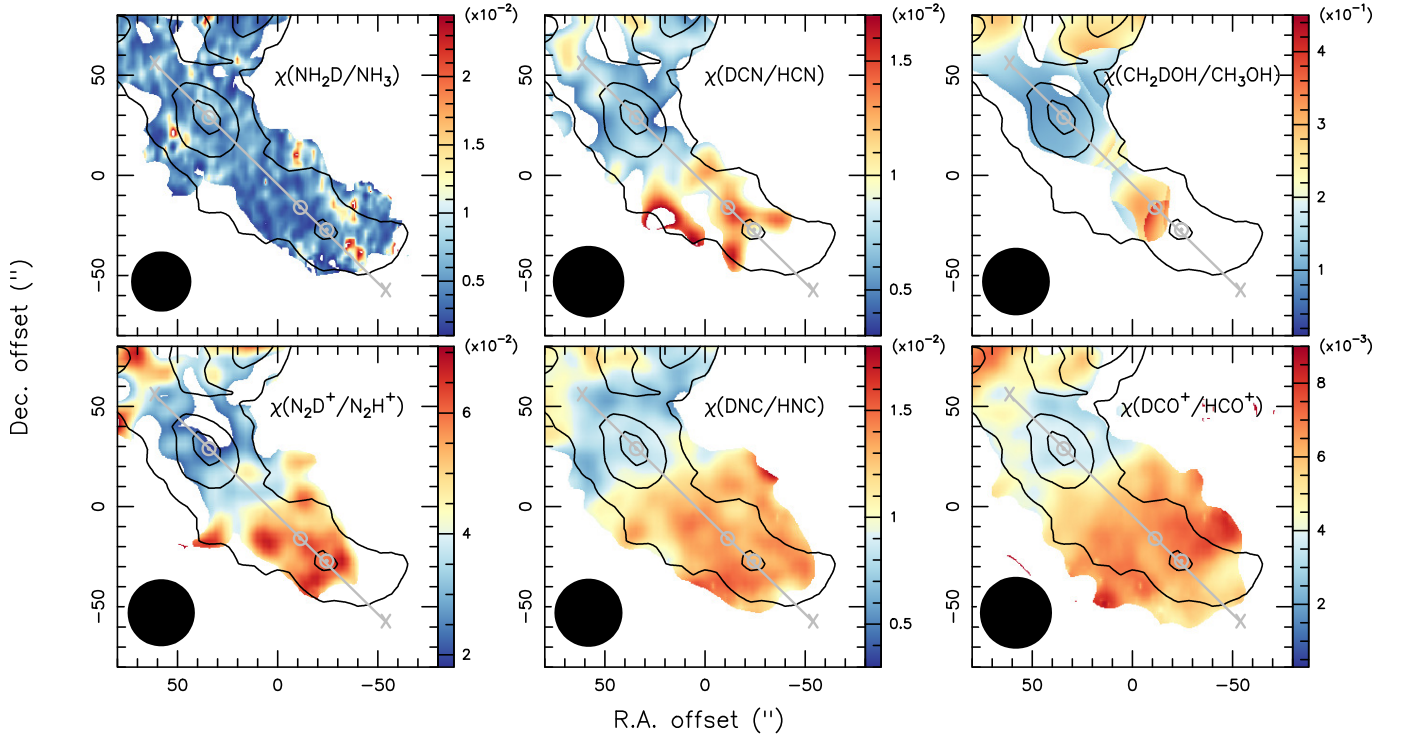


Figure 5. Column density ratio (relative abundance) maps for the deuterated isotopologues with respect to their hydrogenated isotopologues. The column densities of HCN, HNC, and HCO⁺ are converted from those of H¹³CN, HN¹³C, and H¹³CO⁺ by assuming ¹²C/¹³C ~ 42.9. The black contour of 870 μ m continuum emission starts from 10 σ and increases in steps of 10 σ ($\sigma = 0.042$ Jy beam⁻¹). The gray line along the filamentary elongation as well as the position marks on it are the same as in Figure 3. The pixels are blanked where the lines used for calculation have < 3 σ integrated intensity. The angular resolution is shown as the black circle in the bottom left corner.

tions we used in this work may lead to larger systematic uncertainties:

1. *The LTE condition.* The excitation temperatures ($T_{\Delta F}$ and $T_{\Delta J}$) derived for the dense gas tracers, i.e., low- J lines from H¹³CN (DCN), H¹³CO⁺ (DCO⁺), and N₂H⁺ (N₂D⁺), are 5–10 K (Table 2), which is close to their E_u/k_B but lower than the T_{kin} derived from NH₃ (15–20 K, Figure 4), H₂CO, and CH₃OH (> 16 K, Table 3), indicating that these lines are subthermally excited. A feature termed “low excitation temperature” is commonly reported (e.g., Caselli et al. 2002b; Crapsi et al. 2005; Miettinen et al. 2011; Fontani et al. 2012; Gerner et al. 2015). A total column density map for each molecule, based on either the $T_{\Delta J}$ or T_{kin} maps, has an uncertainty of a factor of 2 at each pixel. Nevertheless, the uncertainty does not change the molecular column density gradient along the filamentary elongation from P1 to S. Moreover, such uncertainty can be canceled out when we derive the D-fraction map from the relative abundance ratio of the deuterated molecules with respect to their hydrogenated isotopologues.
2. *Optically thin lines.* We assume that the lines from the ¹⁵N, ¹⁸O, ¹⁷O, and ¹³C hydrogenated molecules

as well as the D-lines of species such as HCN, HNC, HCO⁺ are optically thin. The ¹³C lines, although possibly optically thick toward prestellar cores (e.g., Padovani et al. 2011), are used for deriving the D-fraction maps, which is a compromise for the high-fidelity images covering the entire P1–S region. To test whether the optically thin assumption is valid for the ¹³C lines, we measured the relative abundance ratio $\chi(\text{H}^{15}\text{NC}/\text{HN}^{13}\text{C})$, $\chi(\text{HC}^{15}\text{N}/\text{H}^{13}\text{CN})$, and $\chi(\text{HC}^{18}\text{O}^+/\text{H}^{13}\text{CO}^+)$, and found no variations toward the pixels where both ¹³C line and ¹⁵N/¹⁸O lines show > 3 σ detections (Figure A6). Therefore, even if the ¹³C- lines toward P1–S are optically thick and hence the D-fractions in Figure 5 are upper limits, their optical depths are likely similar toward all pixels in the region we are interested in. Therefore, any gradient found in D-fraction along the filament elongation from P1 to S is a chemical effect rather than an optical depth effect.

3. *The unity beam-filling factor.* Due to the unknown distribution of the molecular lines along the line-of-sight, we assume that all lines we used to derive the molecular column densities have no beam dilution. For NH₃, we found that its column density map from “HfS fit

ting” of the (1,1) and (2, 2) lines shows negligible differences when assuming large or no beam dilution, indicating that the emission of the (1,1) and (2,2) lines is spatially extended at an angular resolution of $\sim 5''$. However, this assumption may not be true for some lines even if we only consider the spatial distribution in the plane of the sky. Taking $\text{CH}_2\text{DOH}(2_{0,2} - 1_{0,1})$ as an example, we find that the region where it is detected with $> 3\sigma$ emission shows a narrow ($\sim 10''$ in width) filamentary morphology. Therefore, the column density of this species may be underestimated.

4. *The fractionation of $^{12}\text{C}/^{13}\text{C}$.* In order to compare the D-fraction of each species derived here with values found in the literatures, we convert the column densities of the ^{13}C isotopologues into those of the ^{12}C isotopologues using the isotopic ratio $\mathcal{R}_{^{12}\text{C}/^{13}\text{C}} = 42.9$ as a conversion factor. This is a statistic value according to the source distance to the Galactic center (Giannetti et al. 2014). However, in an environment like that of the P1–S region, i.e., with dynamic ages of 10^5 yr of the source (Feng et al. 2016c), gas temperatures in the range of 10–20 K, and a number density in the range of $10^4 - 10^5 \text{ cm}^{-3}$, $^{12}\text{C} \rightleftharpoons ^{13}\text{C}$ conversion via isotopic exchange reactions is active. For example, model predictions of the $\mathcal{R}_{^{12}\text{C}/^{13}\text{C}}$ in gaseous HCN, HNC, and H^{13}CO^+ are ~ 80 , ~ 70 , and ~ 47 , respectively, in such an environment (Furuya et al. 2011). Our D-fraction estimates for these species might be overestimated by a factor of 1.5–2.
5. *The OPR for NH_3 and NH_2D .* We assume $\text{OPR} \sim 1$ for NH_3 and $\text{OPR} \sim 3$ for NH_2D in their relative abundance estimation, which may not be true. For example, OPR of NH_2D is reported by modeling of Sipilä et al. (2015) as ~ 2 , and 2.8 by Harju et al. (2017) from observations of the low-mass prestellar core. Nevertheless, this will only add an uncertainty of $< 20\%$.

In short, although the absolute value of the column density for a particular molecule in individual pixels may be underestimated or overestimated based on the above assumptions, we can still trust the gradient shown in the relative abundance ration maps of the deuterated isotopologues with respect to their hydrogenated isotopologues.

5.5. Variations in deuteration for different species

The D-fraction varies for different species. Theoretical studies predict that N_2H^+ and HCO^+ are formed exclusively in the gas phase; HNC and HCN are mainly formed in the gas phase except for very early times; NH_3 and H_2CO are partially formed on the grain surface and partially in the gas phase; while CH_3OH is exclusively form on grain surfaces

(e.g., Parise et al. 2002; Aikawa et al. 2005, 2012; Garrod et al. 2007; Graninger et al. 2014). Table 4 lists the D-fraction of N_2H^+ , HCN, HNC, HCO^+ , NH_3 , and CH_3OH toward P1, S, and Soff. In considering the beam at 1 mm ($\sim 10''$) as well as the gridding kernel of the 3 mm maps (one-third the size of the beam, see Mangum et al. 2007), we give the mean of five parameters, including the D-fraction (D) and its systematic uncertainty for each species, the intensity ratio X and its uncertainty between the lines of deuterated-hydrogenated isotopologues, the gas kinetic temperature T_{kin} , NH_3 column density, and the H_2 column density, toward a $5''$ -radius region centered on P1, S, or Soff. All species in this work, except for NH_3 and CH_3OH , show an enriched deuterium fractionation toward S compared with P1 of a factor of 2–3.

Compared with previous D-fraction studies of the above species toward high-/low-mass star-forming regions, we find that $D(\text{N}_2\text{H}^+)$ observed at an angular resolution of $30''$ is consistent with the results of observations at an angular resolution of $5''$ toward the same source (Chen et al. 2010b, in which P1 is called MM4, and S is called MM9). Quantitatively, $D(\text{N}_2\text{H}^+)$ ranging from 2% to 6% from P1 to S fits the correlation with CO depletion (~ 10 , see Section 6) at the source distance shown toward the low-mass prestellar cores in Crapsi et al. (2005) and Emprechtinger et al. (2009). However, the value is consistent with the mean $D(\text{N}_2\text{H}^+) \sim 4\%$ reported by Fontani et al. (2011) and Gerner et al. (2015) in high-mass protostellar objects rather than the starless objects. This value is similar to the value found in the IRDC deuterium study by Barnes et al. (2016), indicating not only that a protostellar object is embedded in both P1 and S, but also that S is chemically less far evolved than P1.

$D(\text{HCO}^+)$ is also consistent with those found in the high-mass starless clumps or very young high-mass protostellar objects given by Fontani et al. (2014) and Gerner et al. (2015). Moreover, the relative abundance ratio of $\chi(\text{HCO}^+/\text{HC}^{18}\text{O}^+) = \mathcal{R}_{^{12}\text{C}/^{13}\text{C}} \times \chi(\text{H}^{13}\text{C}^{16}\text{O}^+/\text{H}^{12}\text{C}^{18}\text{O}^+) = 143_{-107}^{+214}$ is consistent with $\mathcal{R}_{^{16}\text{O}/^{18}\text{O}} \sim 300$ given by Giannetti et al. (2014) at our source distance to the Galactic Center.

$D(\text{HCN})$ and $D(\text{HNC})$ in our study are consistent with the values toward other $70 \mu\text{m}$ dark clouds (e.g., Bergin et al. 1999; Turner 2001; Lodders 2003; Miettinen et al. 2011; Sakai et al. 2012; Fontani et al. 2014; Gerner et al. 2015). Although theoretical model predicted that gas-phase reactions dominate the formation of both species in a warm-temperature environment (Graninger et al. 2014), we note that the integrated intensity ratio of $\text{DNC}(1-0)$ with respect to $\text{DCN}(1-0)$ is ~ 3 , which is consistent with the results obtained from solid-state experiments on the reaction of D and CN at 10 K by Hiraoka et al. (2006), indicating that our sources are chemically young. Moreover, assuming $\mathcal{R}_{^{12}\text{C}/^{13}\text{C}} \sim 43$, the relative abundance ratios of $\chi(\text{HNC}/\text{H}^{15}\text{NC}) = \mathcal{R}_{^{12}\text{C}/^{13}\text{C}} \times \chi(\text{H}^{14}\text{N}^{13}\text{C}/\text{H}^{15}\text{N}^{12}\text{C})$

and $\chi(\text{HCN}/\text{HC}^{15}\text{N}) = \mathcal{R}_{^{12}\text{C}/^{13}\text{C}} \times \chi(\text{H}^{13}\text{C}^{14}\text{N}/\text{H}^{12}\text{C}^{15}\text{N})$ are 143_{107}^{+214} , which is consistent with $\mathcal{R}_{^{14}\text{N}/^{15}\text{N}}$ reported by Adande & Ziurys (2012); Zeng et al. (2017) and Colzi et al. (2018).

The single $D(\text{NH}_3)$ in the entire region is in general consistent with detections in dense ($> 10^5 \text{ cm}^{-3}$) and cold ($< 20 \text{ K}$) cores (e.g., Pillai et al. 2011; Fontani et al. 2015, 2.3% toward MM9). The slightly lower value (0.3% – 1.9%) in our study is likely due to the fact that the NH_3 observed at an angular resolution of $5''$ traces more deeply embedded gas than that traced by NH_2D at an angular resolution of $30''$. This implies that deeper into clumps P1 and S, the gas temperature should be higher for such a low value of $D(\text{NH}_3)$.

The single $D(\text{CH}_3\text{OH})$ detection is 10% – 39% in a region where $> 3\sigma$ emission of the only detected CH_2DOH line distributes compactly. This value is higher than the upper limit reported by Fontani et al. (2015) toward MM9. In particular, the D-fraction peak toward Soff is higher than that in low-mass prestellar cores ($\sim 10\%$, e.g., Bizzocchi et al. 2014). Instead, it is closer to the value reported in the Class 0 protostars (e.g., Parise et al. 2006) and gas-grain model results applied to protostellar objects (Awad et al. 2014). This may indicate a deeply embedded dense protostellar object(s) toward Soff. An underestimate of the CH_3OH column density can also account for an overestimate of the $D(\text{CH}_3\text{OH})$, as discussed in Section 5.4, but it is not likely the case for such high $D(\text{CH}_3\text{OH})$ here. In fact, checking the location where Fontani et al. (2015) carried out the pointing observation (south of S), we find the singly $D(\text{CH}_3\text{OH})$ is $< 0.3\%$ in our map, which is consistent with their upper limit of 0.4% given by their nondetection of this line. This result also shows the advantage of mapping over pointing observations to study chemistry.

6. THE SPATIAL CORRELATION BETWEEN DEUTERIUM FRACTIONATION AND CO DEPLETION

When comparing the D-fraction maps of each species (Figure 5), we not only confirm the fact that the D-fraction of NH_3 does not increase toward any place along the filamentary elongation from P1 to S, but we also see the clear location where the D-fraction shows the most significant enrichment. Therefore, we define another species-dependent position P_{max} , where we find the D-fraction maximum for individual species. Table 4 lists the mean of gas and dust parameters toward P_{max} ; the maxima of (single) deuterium fractionation for HCN and CH_3OH are toward Soff rather than S.

It is predicted by models such as the model developed by Vasyunin et al. (2017) that CH_3OH is formed on grain surfaces as soon as CO freezes out, and hence more efficient deuterium fractionation of CH_3OH indicates a high abundance of CO on the grain surface. Moreover, the freeze-out

temperature of CO is around 20 K, and the integrated intensity maps of low- J as well as mid- J ^{13}CO , C^{18}O , and C^{17}O show emission peaks $5''$ – $10''$ offset from P1 and S (Feng et al. 2016b; Pon et al. 2016a). Therefore, it is likely that a large portion of CO resides on grain surfaces toward P1, S, and Soff.

According to Frerking et al. (1982), Wilson & Rood (1994), and Giannetti et al. (2014), the expected relative abundance of C^{18}O with respect to H_2 (denoted as $\chi_{\text{C}^{18}\text{O}}^E$) in the P1–S region should be $\chi_{\text{C}^{18}\text{O}}^E = \chi_{^{12}\text{CO}}^E / \mathcal{R}_{^{16}\text{O}/^{18}\text{O}} = 9.50 \times 10^{-5} e^{(1.11-0.13D_{\text{GC}})} / (58.80D_{\text{GC}} + 37.10) \sim 4.97 \times 10^{-7}$.

Gaussian fits to the beam-averaged line profiles of $\text{C}^{18}\text{O}(2-1)$ and $\text{C}^{17}\text{O}(2-1)$ toward P1 and S show similar centroid velocity and FWHM as the lines we study here (Feng et al. 2016b). Therefore, we assume that the contamination from the foreground and background gas to CO is negligible. Low- J CO isotopologue lines are not dense gas tracers, so $\text{C}^{18}\text{O}(2-1)$ shows emission with an S/N > 8 at the system velocity toward all pixels on the map. $\text{C}^{17}\text{O}(2-1)$ can be assumed to be optically thin toward all the pixels within the P1–S region, but its emission has a low S/N (< 3 toward the map edge) in our observations. Given that the relative abundance of C^{17}O with respect to C^{18}O is homogeneous across the P1–S region (Figure A6), we assume that $\text{C}^{18}\text{O}(2-1)$ is optically thin, or at least has the same level of optical depth toward the pixels in the region we are interested in. Using the gas kinetic temperature map T_{kin} , we derived the observed column density map of C^{18}O (Figure 6). Comparing the observed C^{18}O column density map with that obtained from the undepleted CO abundance ($\chi_{\text{C}^{18}\text{O}}^E$) and $\text{N}(\text{H}_2)$ map, we present the C^{18}O depletion map in Figure 6 as well.

Although the C^{18}O depletion in general may be overestimated by our assumption of the gas-to-dust ratio (here we take 150 from Draine 2011) and the optical depth of the (2–1) line, its variation along the filament elongation should be real. That is to say, C^{18}O and then CO is frozen out onto the grains toward the center of P1 and S by a factor of ~ 10 . In particular, we find that the high depletion extends from S to Soff, and this value is consistent with that reported by pointing observations toward both locations (Pon et al. 2016b).

Although high CO depletion (up to ~ 20) has commonly been detected by pointing observations toward the cold and dense cores of IRDCs (with a gas-to-dust ratio assumed to be 100 in Fontani et al. 2012; Giannetti et al. 2014), a parsec-scale CO depletion map and its spatial correlation with the widespread $D(\text{N}_2\text{H}^+)$ map have only been reported in IRDC G035.39-00.33 (e.g., Hernandez et al. 2011; Barnes et al. 2016). Our current work, followed by the study of a larger sample of $70 \mu\text{m}$ dark clouds, unveils that parsec-scale CO depletion is widely detected, showing spatial anti-correlation

Table 4. Deuterium Fraction of Six species at Different Locations

Parameters	o -NH ₂ D/ p -NH ₃	N ₂ D ⁺ /N ₂ H ⁺	DCN/HCN ^a	DNC/HNC ^a	DCO ⁺ /HCO ⁺ ^a	CH ₂ DOH/CH ₃ OH
Hyd. lines used	NH ₃ (J, K)=(1,1), (2,2)	N ₂ H ⁺ (1-0)	H ¹³ CN (1-0), (2-1)	HN ¹³ C (1-0)	H ¹³ CO ⁺ (1-0), (2-1)	lines of CH ₃ OH list in Table 1
$D_{P1}^{b,d,h}$	0.8% ± 0.5%	2.1% ± 0.9%	0.7% ± 0.2%	0.8% ± 0.3%	0.4% ± 0.1%	10.3% ± 8.0%
$D_S^{d,h}$	0.4% ± 0.3%	6.1% ± 2.4%	< 0.3% ⁱ	1.3% ± 0.5%	0.7% ± 0.2%	< 23.0% ⁱ
$D_{Soff}^{c,d,h}$	0.3% ± 0.2%	5.9% ± 2.1%	1.6% ± 0.8%	1.4% ± 0.5%	0.6% ± 0.2%	33.3% ± 26.7%
P_{max}^e (w.r.t. S)	[31'', 24'']	[-7'', 0'']	[11'', 8'']	[2'', -10'']	[-3'', 5'']	[17'', 9'']
$D_{P_{max}}^d$	2.2% ± 1.8%	6.8% ± 3.8%	1.5% ± 0.8%	1.5% ± 0.9%	0.7% ± 0.3%	41.3% ± 33.1%
$N_{dust, P_{max}}^{d,f}$ (cm ⁻²)	4.9 ± 1.2(22)	5.3 ± 0.8(22)	7.0 ± 2.6(22)	4.8 ± 0.8(22)	6.1 ± 1.3(22)	5.8 ± 1.7(22)
$T_{kin, P_{max}}^d$ (K)	19.0 ± 9.5	13.0 ± 5.5	12.3 ± 3.4	9.2 ± 4.6	13.1 ± 3.6	11.6 ± 3.5
$N_{NH_3, P_{max}}^{d,f,g}$ (cm ⁻²)	1.8 ± 1.1(15)	3.0 ± 2.4(15)	7.4 ± 5.9(15)	4.8 ± 3.8(15)	4.0 ± 3.2(15)	6.9 ± 5.5(15)
Line Ratio ^j	$\frac{NH_2D(1_{1,1} 0s-1_{0,1})}{NH_3(1_1 0a-1_1 0s)}$	$\frac{N_2D^+(1-0)}{N_2H^+(1-0)}$	$\frac{DCN(1-0)}{H^{13}CN(1-0)}$	$\frac{DNC(1-0)}{HN^{13}C(1-0)}$	$\frac{DCO^+(1-0)}{H^{13}CO^+(1-0)}$	$\frac{CH_2DOH(2_{0,2}-1_{0,1} e0)}{CH_3OH(2_{0,2}-1_{0,1} A)}$
X_{P1}	2.1% ± 0.3%	1.7% ± 0.5%	21.3% ± 4.8%	35.9% ± 8.9%	33.2% ± 15.7%	0.8% ± 0.2%
X_S	3.5% ± 0.5%	4.4% ± 1.1%	< 10.0% ⁱ	58.3% ± 15.3%	61.8% ± 23.4%	< 1.8% ⁱ
X_{Soff}	3.0% ± 0.5%	4.3% ± 0.9%	44.1% ± 14.6%	60.5% ± 12.7%	59.2% ± 24.1%	2.8% ± 0.8%

Note. ^a Deuterium fraction is derived from the ¹³C lines of the hydrogenated isotopologues

by assuming optically thin lines, the same beam-filling factor, and a constant fraction of ¹²C/¹³C ~ 42.9;

^b The 870 μm dust continuum peak P1 (18^h42^m50^s.289, -04°03'16".492, J2000) is at the offset of [60'', 56''] with respect to S (18^h42^m46^s.358, -04°04'12".559, J2000);

^c The 870 μm dust continuum peak Soff (18^h42^m47^s.240, -04°04'01".37, J2000) is at the offset of [12'', 11''] with respect to S;

^d Values are derived within a region with a radius of 5'' centered on P1, S, Soff, or P_{max};

^e This location shows the maximum D-fraction for a certain species in the region where 870 μm continuum, NH₃ (1,1), and lines from a particular hydrogenated-deuterated isotopologues all show > 3σ emission. We give its coordinate in the format of an offset to S.

^f (x ± y) × 10^z is presented in the form of x ± y(z);

^g The gas column density N_{NH₃} is derived by assuming the filling factor $f \sim 1$;

^h $T_{kin, P1}$, $N_{H_2, P1}$, $N_{NH_3, P1}$ within a radius of 5'' offset around P1 is 18.4 ± 4.5 K, (9.8 ± 1.1) × 10²² cm⁻², (4.2 ± 2.6) × 10¹⁵ cm⁻², respectively;

$T_{kin, Soff}$, $N_{H_2, Soff}$, $N_{NH_3, Soff}$ within a radius of 5'' offset around Soff is 13.7 ± 4.1 K, (7.2 ± 2.1) × 10²² cm⁻², (5.0 ± 3.0) × 10¹⁵ cm⁻², respectively;

$T_{kin, S}$, $N_{H_2, S}$, $N_{NH_3, S}$ within a radius of 5'' offset around S is 12.5 ± 3.6 K, (6.2 ± 2.1) × 10²² cm⁻², (6.7 ± 5.4) × 10¹⁵ cm⁻², respectively;

ⁱ The integrated intensity of the deuterated line toward S has an S/N < 3, we give the upper limit as 3σ.

^j Line ratio in main-beam temperature.

with the deuterium peak of N₂H⁺ and HCO⁺ (S. Feng et al. in prep, Paper II).

7. CONCLUSIONS

Using the IRAM-30m telescope, we carried out an line imaging survey at 1.3 mm–4.3 mm toward two young high-mass star-forming clumps P1 and S, which are 1.8 pc apart in the same 70 μm dark filamentary IRDC G28.34+0.06. The broad bandwidth observations cover several ground-state lines of deuterated and hydrogenated molecules simultaneously. The unique physical structures and evolutionary stages of our sources enable us to study the deuterium fractionation of six species (NH₃, N₂H⁺, HCN, HNC, HCO⁺, and CH₃OH) with improved robustness by canceling out calibration uncertainty.

Our conclusions are as follows:

1. Mapping is more advantageous over pointing observations for a detailed chemistry study. Maps of the D-fraction of different species with high dynamic range allow us not only to verify a general increase/decrease

trend along the filament elongation, but also to precisely determine the location where deuterium fractionation shows the most significant enrichment.

2. Along the filament elongation from P1 to S, the dust temperature and column density have small dynamic ranges. In contrast, the gas kinetic temperature shows a clear decrease and the NH₃ column density shows a clear increase from P1 (~ 20 K, ~ 4 × 10¹⁵ cm⁻²) to S (~ 14 K, ~ 9 × 10¹⁵ cm⁻²), indicating that the differentiations in physical properties dominate the chemical variations between P1 and S.
3. In the cold and dense P1 and S environments, the low- J lines of H¹³CN, HN¹³C, H¹³CO⁺, and N₂H⁺ are subthermally excited. Nevertheless, these lines can reasonably be assumed to be optically thin. For the CH₃OH, the total column density derived from the RD is consistent with that from LVG fitting. Therefore, the gradient or enrichment we see from P1 to S on the D-fraction maps of individual species is real.

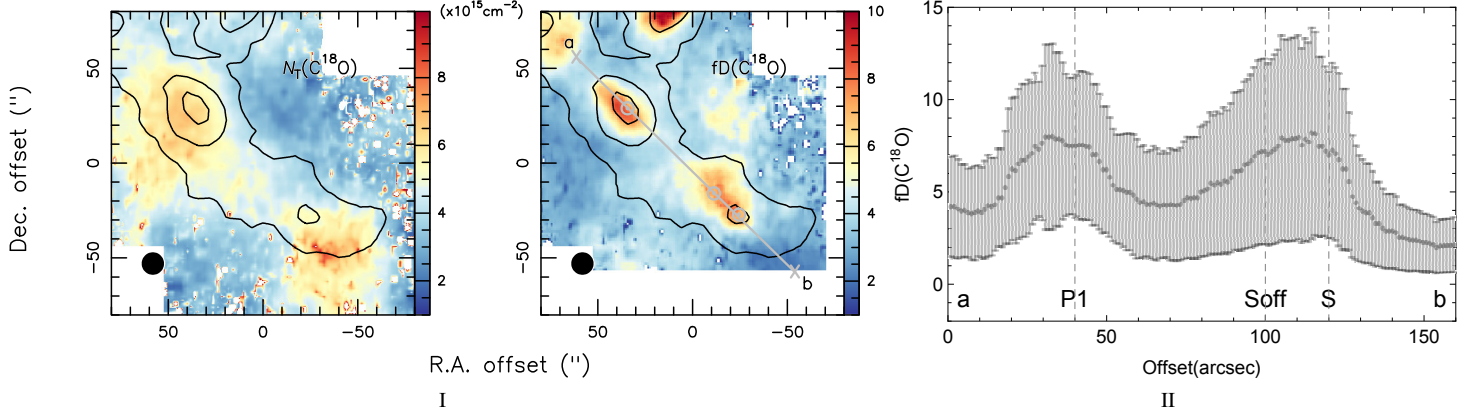


Figure 6. Maps for the $C^{18}O$ column density and depletion. *Panel I:* $C^{18}O$ column density and depletion maps, derived by using the kinetic temperature of the gas and H_2 column density maps (Figure 3 and 4). The angular resolution of $11.8''$ is shown in black in the bottom left. $C^{18}O(2-1)$ shows $> 8\sigma$ emission ($\sigma = 0.11$ K) at the system velocity (79.5 km s^{-1}) toward all pixels on the map. *Panel II:* $C^{18}O$ depletion profile along the directions of a–b (in black). The marked positions are the same as those in Figure 3.

4. The D-fraction of N_2H^+ is several percent in the filament from P1 to S, which is higher than the D-fraction of HCO^+ , HCN, and HNC by an order of magnitude. This is consistent with previous D-fraction studies toward the young protostellar objects in IRDCs. Specifically, D-fraction of these species is higher toward S compared with P1, indicating that deuterium fractionations of these species favor the colder and denser environment, in agreement with previous findings. In contrast, single deuterium fractionation of NH_3 , which forms both in the gas phase and on dust grain surfaces, does not show significant enrichment anywhere on the map.
5. A high level of CO depletion is mapped toward the P1–S region, with the depletion maximum toward P1, S, and Soff ~ 10 . This feature of widespread (parsec-scale) CO depletion is also detected in our follow-up large-sample study of the $70\mu m$ dark clouds.
6. We detect high level of a single D-fraction ($> 10\%$) of CH_3OH toward our source, which was not detected by pointing observations in previous studies. In particular, $D(CH_3OH)$ shows significant enrichment (up to $\sim 40\%$) toward the location $20''$ NE of the continuum peak S, which coincides with the location where CO has the maximum depletion. This is consistent with modeling predictions, where CH_3OH is formed on grain surfaces as soon as CO starts to catastrophically freeze out.
7. G28.34 P1 and S provide us a good space laboratory in which to study the initial chemical condition of HMSF. Because they are neighbors in the same natal cloud, the chemical differentiation is the result of their evolution-

ary stages instead of the external environmental effects (e.g., interstellar UV heating). This comparative study illustrates the potential of measuring the D-fraction of different species as a tool in diagnosing the evolutionary stage of an HMSF region. Observations on a larger sample of IRDCs with similar $70\mu m$ dark/bright source pairs have been carried out to support this pilot study result. Moreover, high-spatial resolution observations are essential to eliminate beam dilution problems, and are key to determine the extremely young protostellar objects embedded in the IRDCs, as well as to understand the correlation between the source evolutionary stage and the deuterium fractionation of different species.

We would like to thank the IRAM-30 m staff for their helpful support during the performance of the IRAM-30 m observations in service mode.

We thank R. Estalella for help with the HfS program.

We thank F. J. Du, Y. Wang, and Z. Y. Zhang for helpful discussions.

S. F. acknowledges the support of the EACOA fellowship from the East Asia Core Observatories Association, which consists of the National Astronomical Observatory of China, the National Astronomical Observatory of Japan, the Academia Sinica Institute of Astronomy and Astrophysics, and the Korea Astronomy and Space Science Institute.

K. W. acknowledges support by the National Key Research and Development Program of China (2017YFA0402702), the National Science Foundation of China (11721303), and the starting grant at the Kavli Institute for Astronomy and Astrophysics, Peking University (7101502016).

H. B. acknowledges support from the European Research Council under the Horizon 2020 Framework Program via the ERC Consolidator Grant CSF-648505.

Software: GILDAS/CLASS (Pety 2005), Hfs (Estalella 2017), PySpecKit (Ginsburg & Mirocha 2011), RADEX (van der Tak et al. 2007)

REFERENCES

- Adande, G. R., & Ziurys, L. M. 2012, *ApJ*, 744, 194, doi: [10.1088/0004-637X/744/2/194](https://doi.org/10.1088/0004-637X/744/2/194)
- Aikawa, Y., Herbst, E., Roberts, H., & Caselli, P. 2005, *ApJ*, 620, 330, doi: [10.1086/427017](https://doi.org/10.1086/427017)
- Aikawa, Y., Wakelam, V., Garrod, R. T., & Herbst, E. 2008, *ApJ*, 674, 984, doi: [10.1086/524096](https://doi.org/10.1086/524096)
- Aikawa, Y., Wakelam, V., Hersant, F., Garrod, R. T., & Herbst, E. 2012, *ApJ*, 760, 40, doi: [10.1088/0004-637X/760/1/40](https://doi.org/10.1088/0004-637X/760/1/40)
- Albertsson, T., Semenov, D. A., Vasyunin, A. I., Henning, T., & Herbst, E. 2013, *ApJS*, 207, 27, doi: [10.1088/0067-0049/207/2/27](https://doi.org/10.1088/0067-0049/207/2/27)
- Ao, Y., Henkel, C., Menten, K. M., et al. 2013, *A&A*, 550, A135, doi: [10.1051/0004-6361/201220096](https://doi.org/10.1051/0004-6361/201220096)
- Awad, Z., Viti, S., Bayet, E., & Caselli, P. 2014, *MNRAS*, 443, 275, doi: [10.1093/mnras/stu1141](https://doi.org/10.1093/mnras/stu1141)
- Bacmann, A., Lefloch, B., Ceccarelli, C., et al. 2003, *ApJL*, 585, L55, doi: [10.1086/374263](https://doi.org/10.1086/374263)
- Barnes, A. T., Kong, S., Tan, J. C., et al. 2016, *MNRAS*, 458, 1990, doi: [10.1093/mnras/stw403](https://doi.org/10.1093/mnras/stw403)
- Barone, V., Latouche, C., Skouteris, D., et al. 2015, *MNRAS*, 453, L31, doi: [10.1093/mnras/slv094](https://doi.org/10.1093/mnras/slv094)
- Battersby, C., Ginsburg, A., Bally, J., et al. 2014, *ApJ*, 787, 113, doi: [10.1088/0004-637X/787/2/113](https://doi.org/10.1088/0004-637X/787/2/113)
- Bergin, E. A., Alves, J., Huard, T., & Lada, C. J. 2002, *ApJL*, 570, L101, doi: [10.1086/340950](https://doi.org/10.1086/340950)
- Bergin, E. A., Plume, R., Williams, J. P., & Myers, P. C. 1999, *ApJ*, 512, 724, doi: [10.1086/306791](https://doi.org/10.1086/306791)
- Beuther, H., & Sridharan, T. K. 2007, *ApJ*, 668, 348, doi: [10.1086/521142](https://doi.org/10.1086/521142)
- Bihl, S., Beuther, H., Linz, H., et al. 2015, *A&A*, 579, A51, doi: [10.1051/0004-6361/201321269](https://doi.org/10.1051/0004-6361/201321269)
- Bizzocchi, L., Caselli, P., Spezzano, S., & Leonardo, E. 2014, *A&A*, 569, A27, doi: [10.1051/0004-6361/201423858](https://doi.org/10.1051/0004-6361/201423858)
- Butler, M. J., & Tan, J. C. 2009, *ApJ*, 696, 484, doi: [10.1088/0004-637X/696/1/484](https://doi.org/10.1088/0004-637X/696/1/484)
- . 2012, *ApJ*, 754, 5, doi: [10.1088/0004-637X/754/1/5](https://doi.org/10.1088/0004-637X/754/1/5)
- Carey, S. J., Noriega-Crespo, A., Mizuno, D. R., et al. 2009, *PASP*, 121, 76, doi: [10.1086/596581](https://doi.org/10.1086/596581)
- Carter, M., Lazareff, B., Maier, D., et al. 2012, *A&A*, 538, A89, doi: [10.1051/0004-6361/201118452](https://doi.org/10.1051/0004-6361/201118452)
- Caselli, P., Benson, P. J., Myers, P. C., & Tafalla, M. 2002a, *ApJ*, 572, 238, doi: [10.1086/340195](https://doi.org/10.1086/340195)
- Caselli, P., Hasegawa, T. I., & Herbst, E. 1993, *ApJ*, 408, 548, doi: [10.1086/172612](https://doi.org/10.1086/172612)
- Caselli, P., Walmsley, C. M., Tafalla, M., Dore, L., & Myers, P. C. 1999, *ApJL*, 523, L165, doi: [10.1086/312280](https://doi.org/10.1086/312280)
- Caselli, P., Walmsley, C. M., Zucconi, A., et al. 2002b, *ApJ*, 565, 344, doi: [10.1086/324302](https://doi.org/10.1086/324302)
- . 2002c, *ApJ*, 565, 331, doi: [10.1086/324301](https://doi.org/10.1086/324301)
- Ceccarelli, C., Caselli, P., Bockelée-Morvan, D., et al. 2014, *Protostars and Planets VI*, 859, doi: [10.2458/azu_uapress_9780816531240-ch037](https://doi.org/10.2458/azu_uapress_9780816531240-ch037)
- Ceccarelli, C., Caselli, P., Herbst, E., Tielens, A. G. G. M., & Caux, E. 2007, in *Protostars and Planets V*, ed. B. Reipurth, D. Jewitt, & K. Keil, 47. <https://arxiv.org/abs/astro-ph/0603018>
- Chen, H.-R., Liu, S.-Y., Su, Y.-N., & Zhang, Q. 2010a, *ApJL*, 713, L50, doi: [10.1088/2041-8205/713/1/L50](https://doi.org/10.1088/2041-8205/713/1/L50)
- . 2010b, *ApJL*, 713, L50, doi: [10.1088/2041-8205/713/1/L50](https://doi.org/10.1088/2041-8205/713/1/L50)
- Chira, R.-A., Beuther, H., Linz, H., et al. 2013, *A&A*, 552, A40, doi: [10.1051/0004-6361/201219567](https://doi.org/10.1051/0004-6361/201219567)
- Colzi, L., Fontani, F., Caselli, P., et al. 2018, *A&A*, 609, A129, doi: [10.1051/0004-6361/201730576](https://doi.org/10.1051/0004-6361/201730576)
- Crapsi, A., Caselli, P., Walmsley, C. M., et al. 2005, *ApJ*, 619, 379, doi: [10.1086/426472](https://doi.org/10.1086/426472)
- Crapsi, A., Caselli, P., Walmsley, C. M., & Tafalla, M. 2007, *A&A*, 470, 221, doi: [10.1051/0004-6361:20077613](https://doi.org/10.1051/0004-6361:20077613)
- Csengeri, T., Bontemps, S., Wyrowski, F., et al. 2017, *A&A*, 600, L10, doi: [10.1051/0004-6361/201629754](https://doi.org/10.1051/0004-6361/201629754)
- Cyganowski, C. J., Whitney, B. A., Holden, E., et al. 2008, *AJ*, 136, 2391, doi: [10.1088/0004-6256/136/6/2391](https://doi.org/10.1088/0004-6256/136/6/2391)
- Draine, B. T. 2003, *ARA&A*, 41, 241, doi: [10.1146/annurev.astro.41.011802.094840](https://doi.org/10.1146/annurev.astro.41.011802.094840)
- . 2011, *Physics of the Interstellar and Intergalactic Medium*
- Emprechtinger, M., Caselli, P., Volgenau, N. H., Stutzki, J., & Wiedner, M. C. 2009, *A&A*, 493, 89, doi: [10.1051/0004-6361:200810324](https://doi.org/10.1051/0004-6361:200810324)
- Estalella, R. 2017, *PASP*, 129, 025003, doi: [10.1088/1538-3873/129/972/025003](https://doi.org/10.1088/1538-3873/129/972/025003)
- Feng, S., Beuther, H., Henning, T., et al. 2015, *A&A*, 581, A71, doi: [10.1051/0004-6361/201322725](https://doi.org/10.1051/0004-6361/201322725)
- Feng, S., Beuther, H., Semenov, D., et al. 2016a, *A&A*, 593, A46, doi: [10.1051/0004-6361/201424912](https://doi.org/10.1051/0004-6361/201424912)
- Feng, S., Beuther, H., Zhang, Q., et al. 2016b, *A&A*, 592, A21, doi: [10.1051/0004-6361/201526864](https://doi.org/10.1051/0004-6361/201526864)
- . 2016c, *ApJ*, 828, 100, doi: [10.3847/0004-637X/828/2/100](https://doi.org/10.3847/0004-637X/828/2/100)
- Feroz, F., & Hobson, M. P. 2008, *MNRAS*, 384, 449, doi: [10.1111/j.1365-2966.2007.12353.x](https://doi.org/10.1111/j.1365-2966.2007.12353.x)

- Feroz, F., Hobson, M. P., & Bridges, M. 2009, *MNRAS*, 398, 1601, doi: [10.1111/j.1365-2966.2009.14548.x](https://doi.org/10.1111/j.1365-2966.2009.14548.x)
- Feroz, F., Hobson, M. P., Cameron, E., & Pettitt, A. N. 2013, arXiv e-prints. <https://arxiv.org/abs/1306.2144>
- Fontani, F., Busquet, G., Palau, A., et al. 2015, *A&A*, 575, A87, doi: [10.1051/0004-6361/201424753](https://doi.org/10.1051/0004-6361/201424753)
- Fontani, F., Caselli, P., Crapsi, A., et al. 2006, *A&A*, 460, 709, doi: [10.1051/0004-6361:20066105](https://doi.org/10.1051/0004-6361:20066105)
- Fontani, F., Giannetti, A., Beltrán, M. T., et al. 2012, *MNRAS*, 423, 2342, doi: [10.1111/j.1365-2966.2012.21043.x](https://doi.org/10.1111/j.1365-2966.2012.21043.x)
- Fontani, F., Sakai, T., Furuya, K., et al. 2014, *MNRAS*, 440, 448, doi: [10.1093/mnras/stu298](https://doi.org/10.1093/mnras/stu298)
- Fontani, F., Palau, A., Caselli, P., et al. 2011, *A&A*, 529, L7, doi: [10.1051/0004-6361/201116631](https://doi.org/10.1051/0004-6361/201116631)
- Frerking, M. A., Langer, W. D., & Wilson, R. W. 1982, *ApJ*, 262, 590, doi: [10.1086/160451](https://doi.org/10.1086/160451)
- Furuya, K., Aikawa, Y., Sakai, N., & Yamamoto, S. 2011, *ApJ*, 731, 38, doi: [10.1088/0004-637X/731/1/38](https://doi.org/10.1088/0004-637X/731/1/38)
- Garrod, R. T., Wakelam, V., & Herbst, E. 2007, *A&A*, 467, 1103, doi: [10.1051/0004-6361:20066704](https://doi.org/10.1051/0004-6361:20066704)
- Gerner, T., Shirley, Y. L., Beuther, H., et al. 2015, *A&A*, 579, A80, doi: [10.1051/0004-6361/201423989](https://doi.org/10.1051/0004-6361/201423989)
- Giannetti, A., Leurini, S., Wyrowski, F., et al. 2017, *A&A*, 603, A33, doi: [10.1051/0004-6361/201630048](https://doi.org/10.1051/0004-6361/201630048)
- Giannetti, A., Wyrowski, F., Brand, J., et al. 2014, *A&A*, 570, A65, doi: [10.1051/0004-6361/201423692](https://doi.org/10.1051/0004-6361/201423692)
- Ginsburg, A., & Mirocha, J. 2011, PySpecKit: Python Spectroscopic Toolkit, Astrophysics Source Code Library. <http://ascl.net/1109.001>
- Ginsburg, A., Henkel, C., Ao, Y., et al. 2016, *A&A*, 586, A50, doi: [10.1051/0004-6361/201526100](https://doi.org/10.1051/0004-6361/201526100)
- Graninger, D. M., Herbst, E., Öberg, K. I., & Vasyunin, A. I. 2014, *ApJ*, 787, 74, doi: [10.1088/0004-637X/787/1/74](https://doi.org/10.1088/0004-637X/787/1/74)
- Harju, J., Daniel, F., Sipilä, O., et al. 2017, *A&A*, 600, A61, doi: [10.1051/0004-6361/201628463](https://doi.org/10.1051/0004-6361/201628463)
- Henshaw, J. D., Caselli, P., Fontani, F., et al. 2016, *MNRAS*, 463, 146, doi: [10.1093/mnras/stw1794](https://doi.org/10.1093/mnras/stw1794)
- Hernandez, A. K., Tan, J. C., Caselli, P., et al. 2011, *ApJ*, 738, 11, doi: [10.1088/0004-637X/738/1/11](https://doi.org/10.1088/0004-637X/738/1/11)
- Hidaka, H., Watanabe, N., Shiraki, T., Nagaoka, A., & Kouchi, A. 2004, *ApJ*, 614, 1124, doi: [10.1086/423889](https://doi.org/10.1086/423889)
- Hiraoka, K., Ushiyama, S., Enoura, T., et al. 2006, *ApJ*, 643, 917, doi: [10.1086/501517](https://doi.org/10.1086/501517)
- Ho, P. T. P., & Townes, C. H. 1983, *ARA&A*, 21, 239, doi: [10.1146/annurev.aa.21.090183.001323](https://doi.org/10.1146/annurev.aa.21.090183.001323)
- Jiménez-Serra, I., Caselli, P., Tan, J. C., et al. 2010, *MNRAS*, 406, 187, doi: [10.1111/j.1365-2966.2010.16698.x](https://doi.org/10.1111/j.1365-2966.2010.16698.x)
- Johnstone, D., Boonman, A. M. S., & van Dishoeck, E. F. 2003, *A&A*, 412, 157, doi: [10.1051/0004-6361:20031370](https://doi.org/10.1051/0004-6361:20031370)
- Jørgensen, J. K., Schöier, F. L., & van Dishoeck, E. F. 2004, *A&A*, 416, 603, doi: [10.1051/0004-6361:20034440](https://doi.org/10.1051/0004-6361:20034440)
- Juvela, M., & Ysard, N. 2011, *ApJ*, 739, 63, doi: [10.1088/0004-637X/739/2/63](https://doi.org/10.1088/0004-637X/739/2/63)
- Kalenskii, S. V., & Kurtz, S. 2016, *Astronomy Reports*, 60, 702, doi: [10.1134/S1063772916080047](https://doi.org/10.1134/S1063772916080047)
- Kong, S., Caselli, P., Tan, J. C., Wakelam, V., & Sipilä, O. 2015, *ApJ*, 804, 98, doi: [10.1088/0004-637X/804/2/98](https://doi.org/10.1088/0004-637X/804/2/98)
- Kong, S., Tan, J. C., Caselli, P., et al. 2018, *ApJ*, 867, 94, doi: [10.3847/1538-4357/aae1b2](https://doi.org/10.3847/1538-4357/aae1b2)
- Leurini, S., Menten, K. M., & Walmsley, C. M. 2016, *A&A*, 592, A31, doi: [10.1051/0004-6361/201527974](https://doi.org/10.1051/0004-6361/201527974)
- Leurini, S., Schilke, P., Menten, K. M., et al. 2004, *A&A*, 422, 573, doi: [10.1051/0004-6361:20047046](https://doi.org/10.1051/0004-6361:20047046)
- Leurini, S., Schilke, P., Wyrowski, F., & Menten, K. M. 2007, *A&A*, 466, 215, doi: [10.1051/0004-6361:20054245](https://doi.org/10.1051/0004-6361:20054245)
- Lin, Y., Liu, H. B., Dale, J. E., et al. 2017, *ApJ*, 840, 22, doi: [10.3847/1538-4357/aa6c67](https://doi.org/10.3847/1538-4357/aa6c67)
- Linsky, J. L., Draine, B. T., Moos, H. W., et al. 2006, *ApJ*, 647, 1106, doi: [10.1086/505556](https://doi.org/10.1086/505556)
- Lodders, K. 2003, *ApJ*, 591, 1220, doi: [10.1086/375492](https://doi.org/10.1086/375492)
- Lucy, L. B. 1974, *AJ*, 79, 745, doi: [10.1086/111605](https://doi.org/10.1086/111605)
- Mangum, J. G., Emerson, D. T., & Greisen, E. W. 2007, *A&A*, 474, 679, doi: [10.1051/0004-6361:20077811](https://doi.org/10.1051/0004-6361:20077811)
- Mangum, J. G., & Shirley, Y. L. 2015, *PASP*, 127, 266, doi: [10.1086/680323](https://doi.org/10.1086/680323)
- Mangum, J. G., & Wootten, A. 1993, *ApJS*, 89, 123, doi: [10.1086/191841](https://doi.org/10.1086/191841)
- Maret, S., Faure, A., Scifoni, E., & Wiesenfeld, L. 2009, *MNRAS*, 399, 425, doi: [10.1111/j.1365-2966.2009.15294.x](https://doi.org/10.1111/j.1365-2966.2009.15294.x)
- Maret, S., Hily-Blant, P., Pety, J., Bardeau, S., & Reynier, E. 2011, *A&A*, 526, A47, doi: [10.1051/0004-6361/201015487](https://doi.org/10.1051/0004-6361/201015487)
- McKee, C. F., & Tan, J. C. 2003, *ApJ*, 585, 850, doi: [10.1086/346149](https://doi.org/10.1086/346149)
- Miettinen, O., Hennemann, M., & Linz, H. 2011, *A&A*, 534, A134, doi: [10.1051/0004-6361/201117187](https://doi.org/10.1051/0004-6361/201117187)
- Millar, T. J., Bennett, A., & Herbst, E. 1989, *ApJ*, 340, 906, doi: [10.1086/167444](https://doi.org/10.1086/167444)
- Molinari, S., Swinyard, B., Bally, J., et al. 2010, *A&A*, 518, L100, doi: [10.1051/0004-6361/201014659](https://doi.org/10.1051/0004-6361/201014659)
- Müller, H. S. P., Schlöder, F., Stutzki, J., & Winnewisser, G. 2005, *Journal of Molecular Structure*, 742, 215, doi: [10.1016/j.molstruc.2005.01.027](https://doi.org/10.1016/j.molstruc.2005.01.027)
- Müller, K. E., Shirley, Y. L., Evans, II, N. J., & Jacobson, H. R. 2002, *ApJS*, 143, 469, doi: [10.1086/342881](https://doi.org/10.1086/342881)
- Oliveira, C. M., Hébrard, G., Howk, J. C., et al. 2003, *ApJ*, 587, 235, doi: [10.1086/368019](https://doi.org/10.1086/368019)
- Ossenkopf, V., & Henning, T. 1994, *A&A*, 291, 943

- Padovani, M., Walmsley, C. M., Tafalla, M., Hily-Blant, P., & Pineau Des Forêts, G. 2011, *A&A*, 534, A77, doi: [10.1051/0004-6361/201117134](https://doi.org/10.1051/0004-6361/201117134)
- Parise, B., Ceccarelli, C., Tielens, A. G. G. M., et al. 2006, *A&A*, 453, 949, doi: [10.1051/0004-6361:20054476](https://doi.org/10.1051/0004-6361:20054476)
- . 2002, *A&A*, 393, L49, doi: [10.1051/0004-6361:20021131](https://doi.org/10.1051/0004-6361:20021131)
- Peretto, N., Fuller, G. A., Duarte-Cabral, A., et al. 2013, *A&A*, 555, A112, doi: [10.1051/0004-6361/201321318](https://doi.org/10.1051/0004-6361/201321318)
- Pety, J. 2005, in *SF2A-2005: Semaine de l'Astrophysique Française*, ed. F. Casoli, T. Contini, J. M. Hameury, & L. Pagani, 721
- Pickett, H. M., Poynter, R. L., Cohen, E. A., et al. 1998, *JQSRT*, 60, 883, doi: [10.1016/S0022-4073\(98\)00091-0](https://doi.org/10.1016/S0022-4073(98)00091-0)
- Pillai, T., Kauffmann, J., Wyrowski, F., et al. 2011, *A&A*, 530, A118, doi: [10.1051/0004-6361/201015899](https://doi.org/10.1051/0004-6361/201015899)
- Pillai, T., Wyrowski, F., Carey, S. J., & Menten, K. M. 2006, *A&A*, 450, 569, doi: [10.1051/0004-6361:20054128](https://doi.org/10.1051/0004-6361:20054128)
- Pon, A., Kaufman, M. J., Johnstone, D., et al. 2016a, *ApJ*, 827, 107, doi: [10.3847/0004-637X/827/2/107](https://doi.org/10.3847/0004-637X/827/2/107)
- Pon, A., Johnstone, D., Caselli, P., et al. 2016b, *A&A*, 587, A96, doi: [10.1051/0004-6361/201527154](https://doi.org/10.1051/0004-6361/201527154)
- Prodanović, T., Steigman, G., & Fields, B. D. 2010, *MNRAS*, 406, 1108, doi: [10.1111/j.1365-2966.2010.16734.x](https://doi.org/10.1111/j.1365-2966.2010.16734.x)
- Rabli, D., & Flower, D. R. 2010, *MNRAS*, 406, 95, doi: [10.1111/j.1365-2966.2010.16671.x](https://doi.org/10.1111/j.1365-2966.2010.16671.x)
- Ragan, S., Henning, T., Krause, O., et al. 2012, *A&A*, 547, A49, doi: [10.1051/0004-6361/201219232](https://doi.org/10.1051/0004-6361/201219232)
- Ragan, S. E., Bergin, E. A., & Gutermuth, R. A. 2009, *ApJ*, 698, 324, doi: [10.1088/0004-637X/698/1/324](https://doi.org/10.1088/0004-637X/698/1/324)
- Ragan, S. E., Bergin, E. A., & Wilner, D. 2011, *ApJ*, 736, 163, doi: [10.1088/0004-637X/736/2/163](https://doi.org/10.1088/0004-637X/736/2/163)
- Ragan, S. E., Henning, T., & Beuther, H. 2013, *A&A*, 559, A79, doi: [10.1051/0004-6361/201321869](https://doi.org/10.1051/0004-6361/201321869)
- Rathborne, J. M., Jackson, J. M., & Simon, R. 2006, *ApJ*, 641, 389, doi: [10.1086/500423](https://doi.org/10.1086/500423)
- Richardson, W. H. 1972, *J. Opt. Soc. Am.*, 62, 55, doi: [10.1364/JOSA.62.000055](https://doi.org/10.1364/JOSA.62.000055)
- Robitaille, T. P., Meade, M. R., Babler, B. L., et al. 2008, *AJ*, 136, 2413, doi: [10.1088/0004-6256/136/6/2413](https://doi.org/10.1088/0004-6256/136/6/2413)
- Rosolowsky, E. W., Pineda, J. E., Foster, J. B., et al. 2008, *ApJS*, 175, 509, doi: [10.1086/524299](https://doi.org/10.1086/524299)
- Sakai, T., Sakai, N., Furuya, K., et al. 2012, *ApJ*, 747, 140, doi: [10.1088/0004-637X/747/2/140](https://doi.org/10.1088/0004-637X/747/2/140)
- Sakai, T., Sakai, N., Kamegai, K., et al. 2008, *ApJ*, 678, 1049, doi: [10.1086/587050](https://doi.org/10.1086/587050)
- Sanhueza, P., Jackson, J. M., Zhang, Q., et al. 2017, *ApJ*, 841, 97, doi: [10.3847/1538-4357/aa6ff8](https://doi.org/10.3847/1538-4357/aa6ff8)
- Schöier, F. L., van der Tak, F. F. S., van Dishoeck, E. F., & Black, J. H. 2005, *A&A*, 432, 369, doi: [10.1051/0004-6361:20041729](https://doi.org/10.1051/0004-6361:20041729)
- Schuller, F., Menten, K. M., Contreras, Y., et al. 2009, *A&A*, 504, 415, doi: [10.1051/0004-6361/200811568](https://doi.org/10.1051/0004-6361/200811568)
- Shirley, Y. L. 2015, *PASP*, 127, 299, doi: [10.1086/680342](https://doi.org/10.1086/680342)
- Shirley, Y. L., Ellsworth-Bowers, T. P., Svoboda, B., et al. 2013, *The Astrophysical Journal Supplement Series*, 209, 2, doi: [10.1088/0067-0049/209/1/2](https://doi.org/10.1088/0067-0049/209/1/2)
- Sipilä, O., Harju, J., Caselli, P., & Schlemmer, S. 2015, *A&A*, 581, A122, doi: [10.1051/0004-6361/201526468](https://doi.org/10.1051/0004-6361/201526468)
- Sokolov, V., Wang, K., Pineda, J. E., et al. 2018, *A&A*, 611, L3, doi: [10.1051/0004-6361/201832746](https://doi.org/10.1051/0004-6361/201832746)
- Sridharan, T. K., Beuther, H., Saito, M., Wyrowski, F., & Schilke, P. 2005, *ApJL*, 634, L57, doi: [10.1086/498644](https://doi.org/10.1086/498644)
- Svoboda, B. E., Shirley, Y. L., Battersby, C., et al. 2016, *ApJ*, 822, 59, doi: [10.3847/0004-637X/822/2/59](https://doi.org/10.3847/0004-637X/822/2/59)
- Tan, J. C., Beltrán, M. T., Caselli, P., et al. 2014, *Protostars and Planets VI*, 149, doi: [10.2458/azu_uapress_9780816531240-ch007](https://doi.org/10.2458/azu_uapress_9780816531240-ch007)
- Tan, J. C., Kong, S., Zhang, Y., et al. 2016, *ApJL*, 821, L3, doi: [10.3847/2041-8205/821/1/L3](https://doi.org/10.3847/2041-8205/821/1/L3)
- Tang, X. D., Henkel, C., Menten, K. M., et al. 2018, *A&A*, 609, A16, doi: [10.1051/0004-6361/201731849](https://doi.org/10.1051/0004-6361/201731849)
- Teyssier, D., Hennebelle, P., & Pérault, M. 2002, *A&A*, 382, 624, doi: [10.1051/0004-6361:20011646](https://doi.org/10.1051/0004-6361:20011646)
- Turner, B. E. 2001, *ApJS*, 136, 579, doi: [10.1086/322536](https://doi.org/10.1086/322536)
- van der Tak, F. F. S., Black, J. H., Schöier, F. L., Jansen, D. J., & van Dishoeck, E. F. 2007, *A&A*, 468, 627, doi: [10.1051/0004-6361:20066820](https://doi.org/10.1051/0004-6361:20066820)
- Vastel, C., Phillips, T. G., Caselli, P., Ceccarelli, C., & Pagani, L. 2006, *Philosophical Transactions of the Royal Society of London Series A*, 364, 3081, doi: [10.1098/rsta.2006.1880](https://doi.org/10.1098/rsta.2006.1880)
- Vasyunin, A. I., Caselli, P., Dulieu, F., & Jiménez-Serra, I. 2017, *ApJ*, 842, 33, doi: [10.3847/1538-4357/aa72ec](https://doi.org/10.3847/1538-4357/aa72ec)
- Vasyunina, T., Linz, H., Henning, T., et al. 2011, *A&A*, 527, A88, doi: [10.1051/0004-6361/201014974](https://doi.org/10.1051/0004-6361/201014974)
- Walmsley, C. M., & Ungerechts, H. 1983, *A&A*, 122, 164
- Wang, K. 2015, *The Earliest Stages of Massive Clustered Star Formation: Fragmentation of Infrared Dark Clouds*, doi: [10.1007/978-3-662-44969-1](https://doi.org/10.1007/978-3-662-44969-1)
- . 2018, *Research Notes of the American Astronomical Society*, 2, 52, doi: [10.3847/2515-5172/aacb29](https://doi.org/10.3847/2515-5172/aacb29)
- Wang, K., Zhang, Q., Wu, Y., Li, H.-b., & Zhang, H. 2012, *ApJL*, 745, L30, doi: [10.1088/2041-8205/745/2/L30](https://doi.org/10.1088/2041-8205/745/2/L30)
- Wang, K., Zhang, Q., Wu, Y., & Zhang, H. 2011, *ApJ*, 735, 64, doi: [10.1088/0004-637X/735/1/64](https://doi.org/10.1088/0004-637X/735/1/64)
- Wang, K., Zhang, Q., Testi, L., et al. 2014, *MNRAS*, 439, 3275, doi: [10.1093/mnras/stu127](https://doi.org/10.1093/mnras/stu127)
- Wang, Y., Zhang, Q., Pillai, T., Wyrowski, F., & Wu, Y. 2008, *ApJL*, 672, L33, doi: [10.1086/524949](https://doi.org/10.1086/524949)
- Watanabe, N., & Kouchi, A. 2002, *ApJ*, 571, L173, doi: [10.1086/341412](https://doi.org/10.1086/341412)

Wienen, M., Wyrowski, F., Schuller, F., et al. 2012, A&A, 544, A146, doi: [10.1051/0004-6361/201118107](https://doi.org/10.1051/0004-6361/201118107)

Wilson, T. L., & Rood, R. 1994, ARA&A, 32, 191, doi: [10.1146/annurev.aa.32.090194.001203](https://doi.org/10.1146/annurev.aa.32.090194.001203)

Woon, D. E. 2002, ApJ, 569, 541, doi: [10.1086/339279](https://doi.org/10.1086/339279)

Zeng, S., Jiménez-Serra, I., Cosentino, G., et al. 2017, A&A, 603, A22, doi: [10.1051/0004-6361/201630210](https://doi.org/10.1051/0004-6361/201630210)

Zhang, Q., Wang, K., Lu, X., & Jiménez-Serra, I. 2015, ApJ, 804, 141, doi: [10.1088/0004-637X/804/2/141](https://doi.org/10.1088/0004-637X/804/2/141)

APPENDIX

A. MODIFIED BLACKBODY FITTING FOR N(H₂) AND T(DUST) MAPS

We assume a dust opacity law of $\kappa_\nu = \kappa_{230}(\frac{\nu}{230\text{GHz}})^\beta$, where $\kappa_{230} = 0.899\text{ cm}^2\text{ g}^{-1}$ (Ossenkopf & Henning 1994). The flux density S_ν at the frequency of ν can be given as $S_\nu = \Omega_m B_\nu(T_d)(1 - e^{-\tau_\nu})$ from the single-component modified blackbody model, where Ω_m is the solid angle of the beam. The H₂ column density can therefore be derived as $N(\text{H}_2) = R \frac{\tau_\nu}{\kappa_\nu \mu_{ISM} m_H}$, where μ_{ISM} is the mean molecular weight in the ISM, which is assumed to be 2.33; m_H is the mass of an hydrogen atom ($1.67 \times 10^{-24}\text{ g}$); and the isothermal gas-to-dust mass ratio R is taken to be 150 (Draine 2003).

To derive the H₂ column density and dust temperature maps, we adopt the following iterative procedure pixel by pixel:

- (1) Assuming $\beta \sim 1.8$, we derive a continuum image at $850\text{ }\mu\text{m}$ from the extrapolation of *Herschel* PACS $70\text{ }\mu\text{m}$, $160\text{ }\mu\text{m}$, and SPIRE $250\text{ }\mu\text{m}$, $350\text{ }\mu\text{m}$, and $500\text{ }\mu\text{m}$ images.
- (2) Using this extrapolated $850\text{ }\mu\text{m}$ continuum image as a model, we deconvolved the Planck 353 GHz image using Lucy-Richardson method (Richardson 1972; Lucy 1974); the deconvolved image has an angular resolution close to the SPIRE $500\text{ }\mu\text{m}$ image ($37''$). The deconvolved image is combined with the *JCMT-SCUBA2* $850\text{ }\mu\text{m}$ map, achieving an angular resolution of $14''$.
- (3) We fit the SED by using the *Herschel* PACS $70\text{ }\mu\text{m}$, $160\text{ }\mu\text{m}$, SPIRE $250\text{ }\mu\text{m}$ maps, the $850\text{ }\mu\text{m}$ map derived from step (2), and the $350\text{ }\mu\text{m}$ map by combining *Herschel* SPIRE and *CSO/SHARC-II*. At an angular resolution of $22''$, we obtain a β map.
- (4) Assuming the β map has no local variation from $22''$ to $10''$ resolution, we apply the Monte Carlo method and fit N(H₂) and T(dust) simultaneously by using the *CSO/SHARC-II* $350\text{ }\mu\text{m}$ and *Herschel* PACS $70\text{ }\mu\text{m}$ emission maps at an angular resolution of $10''$. Assuming a global flux error as 5σ for each continuum map, we take N(H₂) and T(dust) as well as their 1σ as uncertainty from the PDF.

The detailed combination and SED fitting procedures are given in Lin et al. (2017).

B. FIGURES

Figure A1 and A2 show the H₂CO lines and the CH₃OH lines we use to measure the gas temperature in G28.34 P1–S. Figure A3 takes the A-CH₃OH lines toward P1 as an example, and illustrates the probability density function (PDF) of parameters we derive using the LVG method. Figure A4 shows the temperature profiles and column density profiles of *p*-H₂CO and CH₃OH, extracted from the elongation and perpendicular directions of the G28.34 P1–S filament. Figure A5 shows the profiles of D-fraction for six species, extracted from the G28.34 P1–S filament elongation. Figure A6 gives the relative abundance ratios between the ¹⁸O and ¹⁵N isotopologues with respect to their ¹⁶O and ¹⁴N isotopologues.

C. TABLES

Table A1 and A2 list the line profile fitting results using GAUSS or HFS method toward P1 and S. Table A3 lists the measured molecular column densities toward P1, S, and Soff.

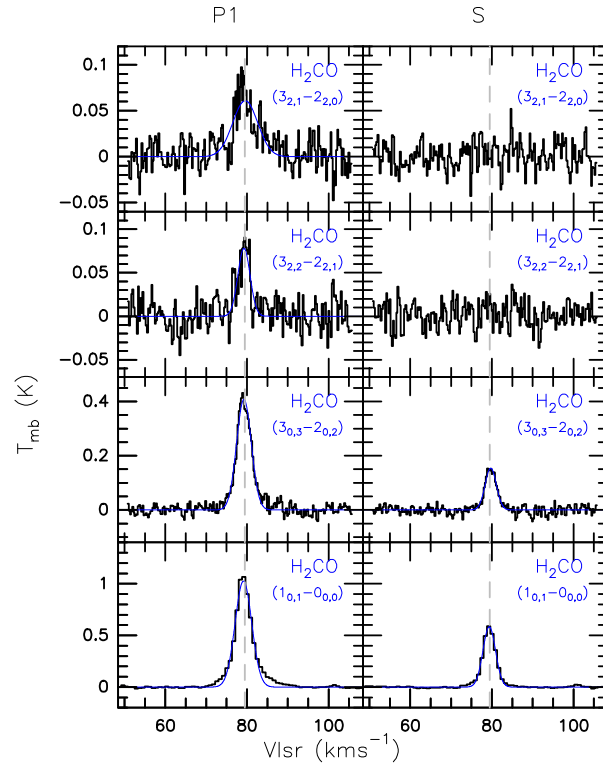


Figure A1. Line profiles of identified p -H₂CO lines toward G28.34 P1–S, averaged from a beam-sized region with the center on P1 and S in the plane of the sky. All p -H₂CO lines are extracted from images smoothed to the same pixel size and angular resolution (35.6"). The best-fit parameters from GAUSS method are given in Table A2. The system velocity (79.5 km s⁻¹) is shown as gray dashed line in each panel.

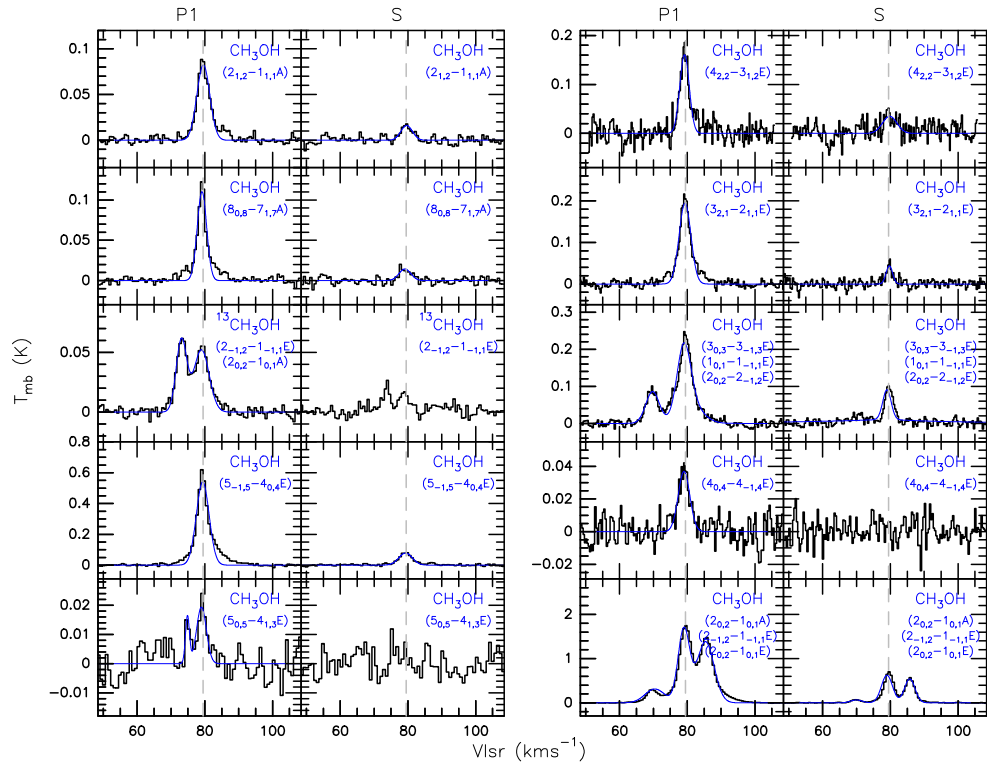
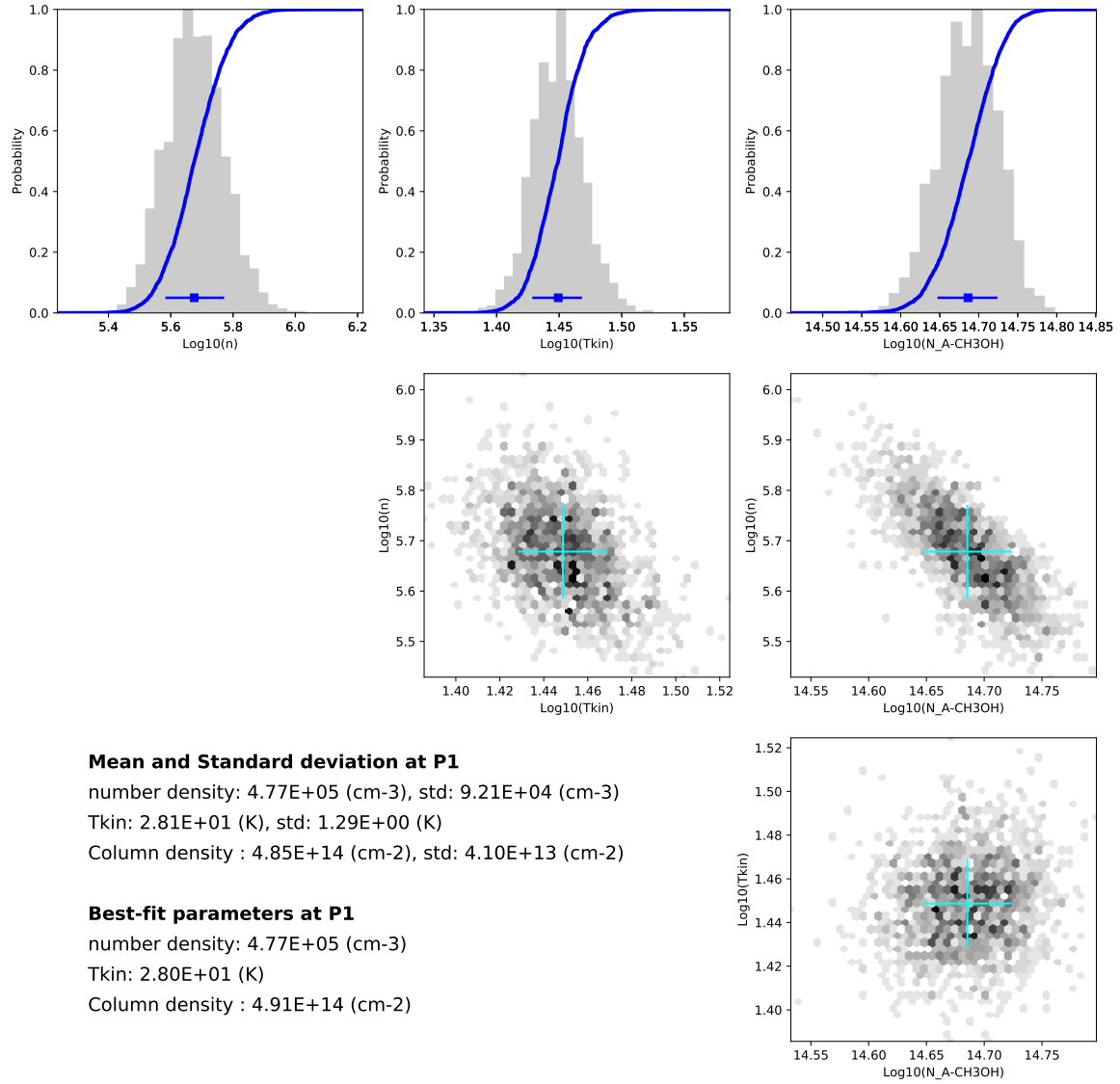


Figure A2. Line profiles of the identified CH_3OH lines toward G28.34 P1–S. The line intensity given in the main-beam temperature is averaged from a beam-sized region with the center on P1 or S in the plane of the sky. All CH_3OH line images are smoothed to the same pixel size and angular resolution ($33.9''$). The best-fit parameters are given by using the GAUSS method, and the parameters are given in Table A2. The system velocity (79.5 km s^{-1}) is shown as a gray dashed line in each panel.



I

Figure A3. The probability density function (PDF) of A-CH₃OH parameters toward P1, derived by using RADEX and MultiNest Algorithm. The fitting parameters, including the H₂ number density n , CH₃OH column density $N(\text{A-CH}_3\text{OH})$, the gas kinetic temperature T_{kin} are listed.

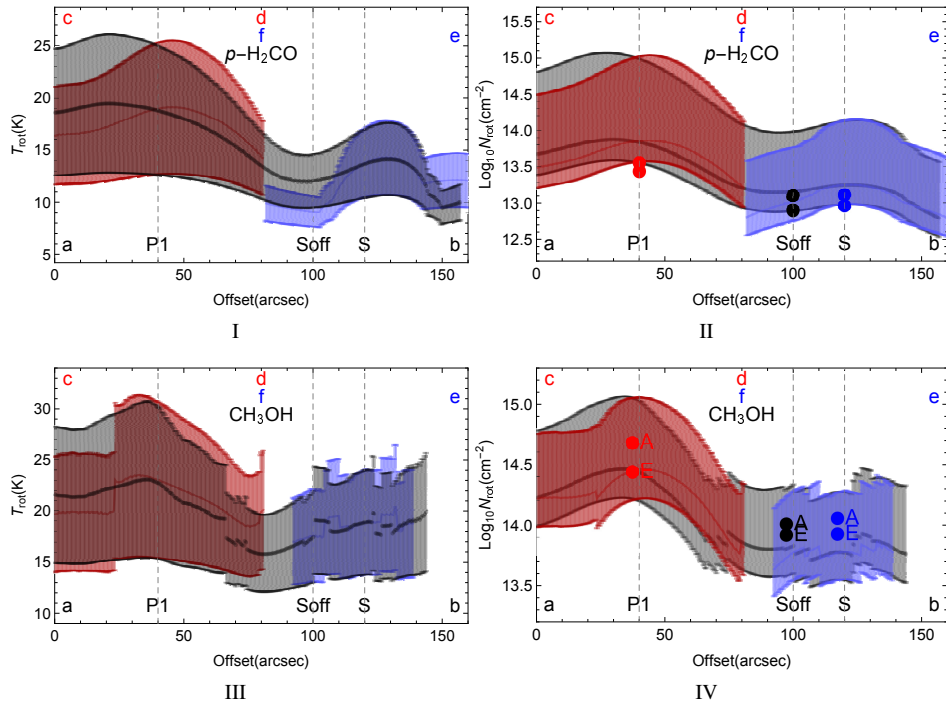


Figure A4. *Panel I–II:* Profiles of the rotation temperature T_{rot} and column density N_{rot} of $p\text{-H}_2\text{CO}$, extracted along the directions of a–b (in black), c–d (in red), and e–f (in blue) in their maps. *Panel III–IV:* Profiles of the rotation temperature T_{rot} and column density N_{rot} of CH_3OH , extracted along the directions of a–b (in black), c–d (in red), and e–f (in blue) in their maps. The labeled positions are the same as those in Figure 3. The red, black, and blue dots indicate the upper and lower limits of column density toward P1, S, and Soff given by LVG fitting. The pixels where any of the $p\text{-H}_2\text{CO}$ or CH_3OH lines show $< 3\sigma$ integrated intensity are blanked.

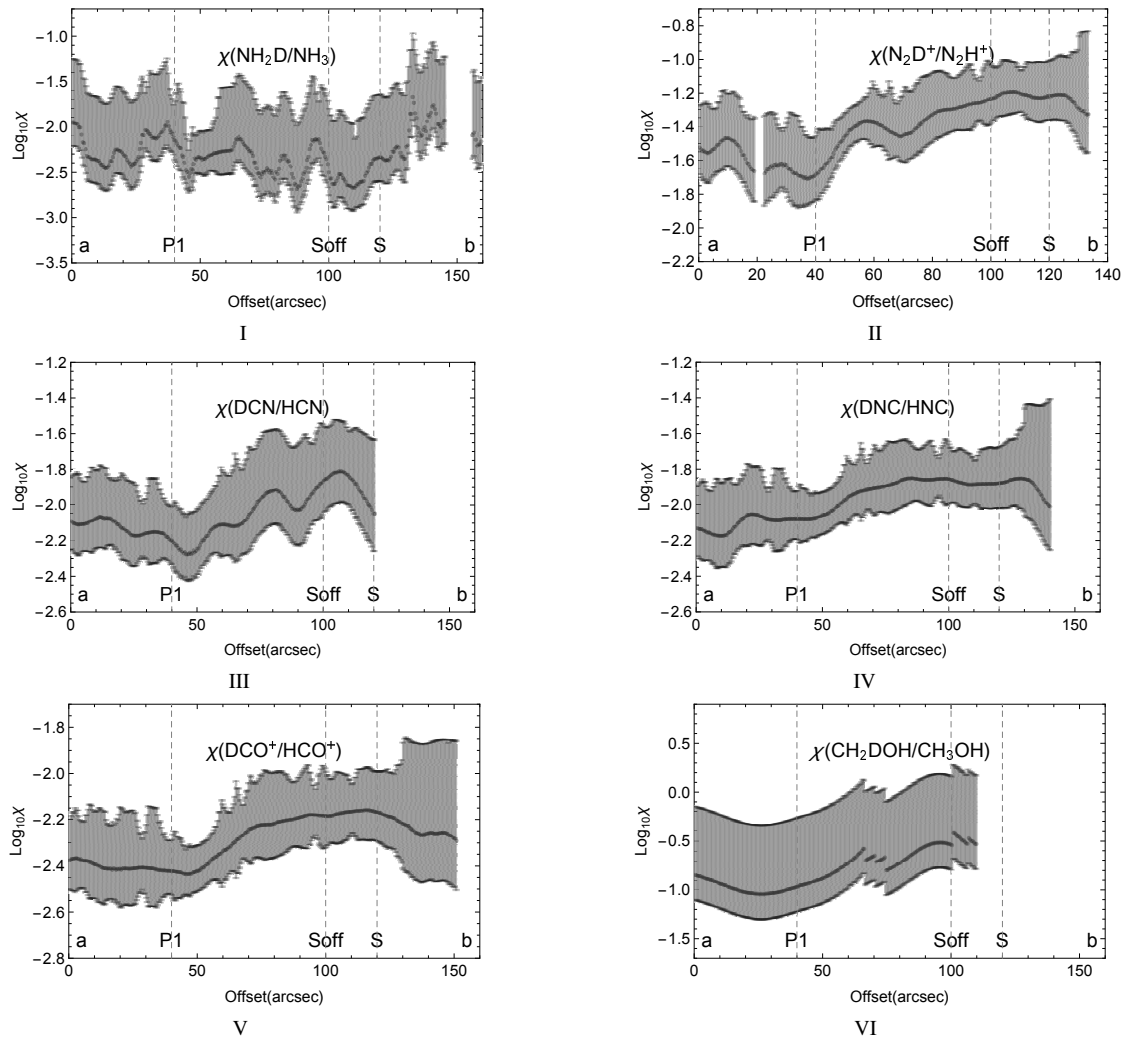


Figure A5. Profile of the relative abundance ratio of the deuterated species with respect to their hydrogenated isotopologues, extracted along the filamentary elongation from a to b in their maps (shown as the gray line in Figure 5). The labeled positions are the same as those in Figure 3. The pixels where the lines used for calculation show $< 3\sigma$ integrated intensity are blanked.

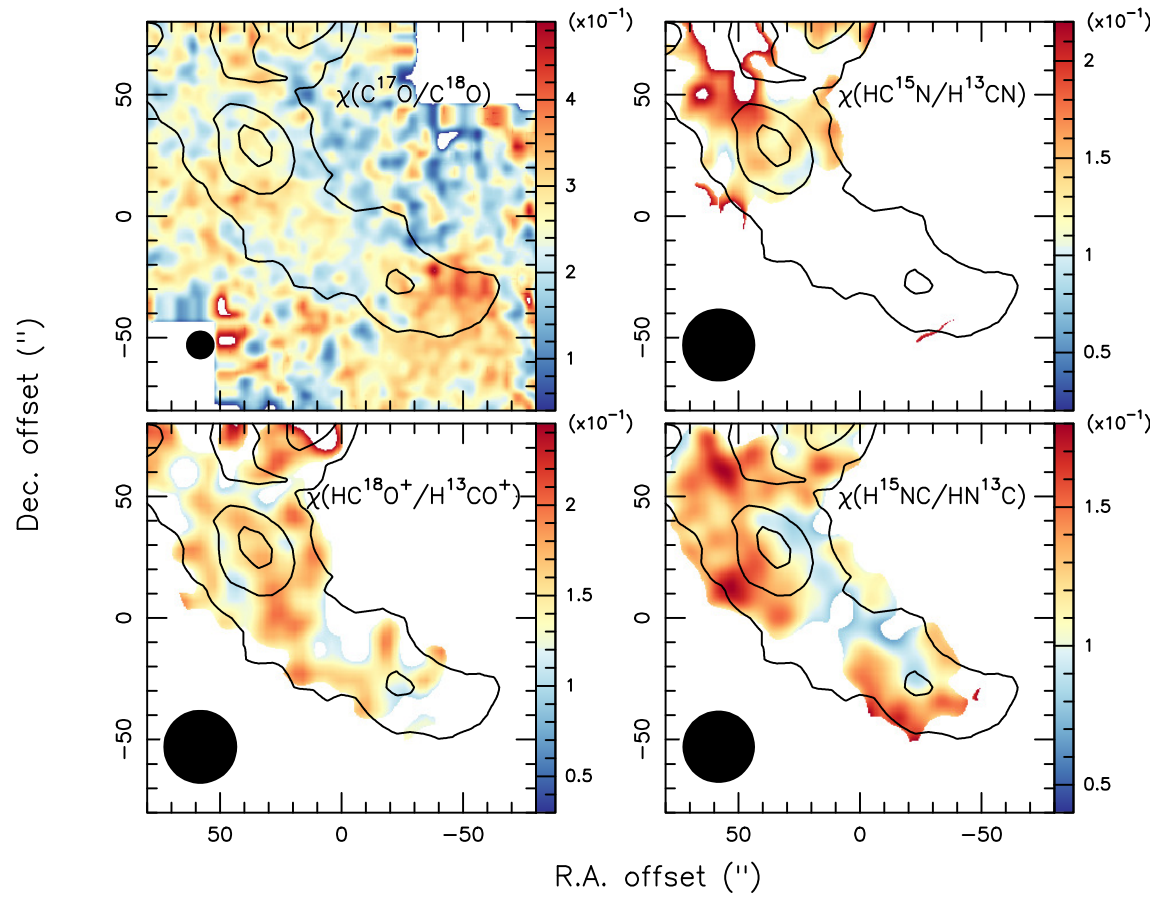


Figure A6. Relative abundance ratio maps of the ^{15}N or ^{18}O isotopologues with respect to their ^{13}C isotopologues. The values derived by using the temperature map of T_{kin} (given here) or T_{Δ} are the same. The pixels where the HC^{15}N (1–0), H^{15}NC (1–0), or HC^{18}O^+ (1–0) line show $< 3\sigma$ integrated intensity are blanked.

Table A1. The best-fit parameters for lines in Figure 1, given by GILDAS.

Line	Freq	P1		S		P1-S
I. line width $\Delta\nu$ (km s ⁻¹) and integrated intensity $\int T_B(\nu)d\nu$ (K km s ⁻¹) ^{a,d,f}						
	(GHz)	(km s ⁻¹)	(K km s ⁻¹)	(km s ⁻¹)	(K km s ⁻¹)	[km s ⁻¹ , km s ⁻¹] ^g
HC ¹⁵ N (1 - 0)	86.055	3.3 ± 0.2	0.18 ± 0.01	3.0 ± 0.4	0.08 ± 0.01	[76, 90]
HN ¹³ C (1 - 0)	87.091	3.6 ± 0.0	1.51 ± 0.01	3.0 ± 0.0	0.99 ± 0.01	[74, 83]
H ¹⁵ NC (1 - 0)	88.866	3.3 ± 0.2	0.18 ± 0.01	2.9 ± 0.2	0.11 ± 0.01	[74, 83]
DNC (1 - 0)	76.306	3.6 ± 0.1	0.55 ± 0.01	3.1 ± 0.1	0.49 ± 0.01	[74, 83]
H ¹³ CO ⁺ (1 - 0) ^c	86.754	3.7 ± 0.0	1.76 ± 0.01	3.2 ± 0.0	1.26 ± 0.01	[74, 83]
HC ¹⁸ O ⁺ (1 - 0)	85.162	3.4 ± 0.2	0.25 ± 0.01	2.2 ± 0.2	0.14 ± 0.01	[74, 83]
DCO ⁺ (1 - 0) ^c	72.039	3.7 ± 0.1	0.61 ± 0.01	3.0 ± 0.1	0.62 ± 0.01	[74, 83]
H ¹³ CO ⁺ (2 - 1) ^c	173.507	2.9 ± 0.1	1.26 ± 0.03	3.0 ± 0.2	0.69 ± 0.04	[74, 83]
CH ₃ OH (2 _{0,2} - 1 _{0,1} A)	96.741	3.9 ± 0.1	8.07 ± 0.17	3.8 ± 0.0	2.95 ± 0.02	[77, 83]
CH ₂ DOH (2 _{0,2} - 1 _{0,1} e0)	89.408	4.0 ± 0.6	0.10 ± 0.01	3.6 ± 0.7	0.06 ± 0.01	[77, 83]
II. line width $\Delta\nu$ (km s ⁻¹) and optical-depth-corrected integrated intensity $A\tau_0\Delta\nu$ (K km s ⁻¹) of the main hyperfine line ^{b,d,f}						
	(GHz) ^e	(km s ⁻¹)	(K km s ⁻¹)	(km s ⁻¹)	(K km s ⁻¹)	[km s ⁻¹ , km s ⁻¹] ^g
NH ₃ (J, K = 1, 1)	23.694	2.3 ± 0.0	16.51 ± 0.51	2.0 ± 0.0	18.65 ± 0.43	[66, 88]
NH ₂ D (J, K = 1, 0)	85.926	2.5 ± 0.3	0.08 ± 0.02	3.0 ± 0.2	0.10 ± 0.01	[66, 88]
H ¹³ CN (1 - 0)	86.340	4.1 ± 0.1	0.24 ± 0.00	3.2 ± 0.1	0.14 ± 0.00	[66, 88]
H ¹³ CN (2 - 1)	172.678	5.6 ± 0.4	0.10 ± 0.01	3.4 ± 0.6	0.05 ± 0.01	[66, 88]
DCN (1 - 0)	72.415	3.4 ± 0.2	0.06 ± 0.00	2.4 ± 0.3	0.06 ± 0.02	[66, 88]
N ₂ H ⁺ (1 - 0)	93.174	3.6 ± 0.0	1.24 ± 0.00	3.0 ± 0.0	0.86 ± 0.00	[68, 91]
N ₂ D ⁺ (1 - 0)	77.110	2.4 ± 0.2	0.05 ± 0.01	2.7 ± 0.2	0.03 ± 0.00	[68, 91]
N ₂ D ⁺ (2 - 1)	154.217	2.7 ± 0.6	0.03 ± 0.01	2.3 ± 0.3	0.04 ± 0.01	[68, 91]
H ¹³ CO ⁺ (1 - 0) ^c	86.754	3.5 ± 0.1	0.21 ± 0.00	2.8 ± 0.1	0.25 ± 0.02	[74, 83]
DCO ⁺ (1 - 0) ^c	72.039	2.3 ± 0.1	0.51 ± 0.12	2.5 ± 0.2	0.20 ± 0.05	[74, 83]
H ¹³ CO ⁺ (2 - 1) ^c	173.506	2.8 ± 0.1	0.16 ± 0.00	1.9 ± 0.1	0.43 ± 0.12	[74, 83]

Note. *a.* Subtable I lists the parameters of a single unblended line or the strongest line when several lines at different transitions are not completely resolved by our observations. Lines are fitted using the GAUSS method.

b. Subtable II lists the parameters of the main line taking into account the hyperfine structure. Lines are fitted using the HFS method.

The excitation temperature of the hyperfine splitting $T_{\Delta F}$ can be derived from $A\tau_0$ and τ_0 , as $T_{\Delta F} = \frac{h\nu/k_B}{\ln[\frac{h\nu/k_B}{A\tau_0(\tau_0)^{-1} + 1}]}$.

c. Hyperfine splittings are recorded in JPL or CDMS but are not resolved in observations. Line is fitted by using both GAUSS and HFS.

d. Lines are extracted from images by averaging a beam-sized region centered at 870 μm continuum peak P1 or S in the plane of the sky.

All line images have the same pixel size, but their angular resolutions were the same as in the observations without smoothing (Table 1).

e. The rest frequency is given from the main line of the hyperfine splittings.

f. Uncertainties on the measured intensities are typically $\leq 10\%$.

g. This column lists the velocity range we integrate for individual lines to obtain their intensity maps in Figure 2.

Table A2. The best-fit parameters for H₂CO lines in Figure A1 and for CH₃OH lines in Figure A2, given by GILDAS

Line ^{a,b}	Freq (GHz)	P1		S		P1-S [km s ⁻¹ , km s ⁻¹] ^{e,f,i}
		Δv (km s ⁻¹) ^c	$\int T_B(v)dv$ (K km s ⁻¹) ^c	Δv (km s ⁻¹) ^{c,d}	$\int T_B(v)dv$ (K km s ⁻¹) ^{c,d}	
H ₂ CO (1 _{0,1} – 0 _{0,0})	72.838	4.8 ± 0.1	5.25 ± 0.05	3.6 ± 0.0	2.25 ± 0.02	[74, 83]
H ₂ CO (3 _{0,3} – 2 _{0,2})	218.222	4.2 ± 0.1	1.84 ± 0.03	3.2 ± 0.2	0.53 ± 0.02	[74, 83]
H ₂ CO (3 _{2,2} – 2 _{2,1})	218.476	3.5 ± 0.4	0.29 ± 0.03	---	$\sigma = 0.09$	[74, 83]
H ₂ CO (3 _{2,1} – 2 _{2,0})	218.760	7.2 ± 1.0	0.47 ± 0.04	---	$\sigma = 0.06$	[74, 83]
CH ₃ OH (5 _{0,5} – 4 _{1,3} E)	76.510	3.4 ± 1.6	0.07 ± 0.02	---	$\sigma = 0.01$	--- ^f
CH ₃ OH (5 _{-1,5} – 4 _{0,4} E)	84.521	4.5 ± 0.1	2.56 ± 0.05	4.7 ± 0.3	0.39 ± 0.02	[74, 84]
¹³ CH ₃ OH (2 _{-1,2} – 1 _{-1,1} E)	94.405	5.3 ± 0.2	0.30 ± 0.01	---	$\sigma = 0.11$	--- ^f
¹³ CH ₃ OH (2 _{0,2} – 1 _{0,1} A)	94.407	3.7 ± 0.1	0.24 ± 0.00	---	$\sigma = 0.11$	--- ^f
CH ₃ OH (8 _{0,8} – 7 _{1,7} A)	95.169	3.3 ± 0.2	0.38 ± 0.01	4.1 ± 0.7	0.06 ± 0.01	[74, 84]
CH ₃ OH (2 _{1,2} – 1 _{1,1} A)	95.914	4.5 ± 0.2	0.39 ± 0.01	4.0 ± 0.6	0.07 ± 0.01	[74, 84]
CH ₃ OH (2 _{-1,2} – 1 _{-1,1} E)	96.739	6.8 ± 0.6	2.28 ± 0.35	3.9 ± 0.3	0.27 ± 0.01	[82, 95] ^g
CH ₃ OH (2 _{0,2} – 1 _{0,1} A)	96.741	4.0 ± 0.6	7.08 ± 0.35	3.8 ± 0.0	2.56 ± 0.01	[73, 82] ^g
CH ₃ OH (2 _{0,2} – 1 _{0,1} E)	96.745	5.9 ± 0.6	8.74 ± 0.35	3.6 ± 0.0	2.09 ± 0.02	[65, 73] ^g
CH ₃ OH (4 _{0,4} – 4 _{-1,4} E)	157.246	4.1 ± 0.5	0.16 ± 0.01	---	$\sigma = 0.04$	---
CH ₃ OH (3 _{0,3} – 3 _{-1,3} E)	157.270	4.8 ± 0.1	0.89 ± 0.02	2.9 ± 0.2	0.25 ± 0.02	[77, 88] ^h
CH ₃ OH (1 _{0,1} – 1 _{-1,1} E)	157.271	4.7 ± 0.3	0.43 ± 0.02	5.71 ± 3.98	0.43 ± 0.00	[72, 77] ^h
CH ₃ OH (2 _{0,2} – 2 _{-1,2} E)	157.276	8.3 ± 0.8	0.43 ± 0.02	5.6 ± 2.1	0.05 ± 0.00	[64, 72] ^h
CH ₃ OH (3 _{2,1} – 2 _{1,1} E)	170.061	4.1 ± 0.1	0.85 ± 0.02	2.3 ± 0.5	0.10 ± 0.02	[74, 84]
CH ₃ OH (4 _{2,2} – 3 _{1,2} E)	218.440	3.3 ± 0.2	0.56 ± 0.03	5.0 ± 1.0	0.19 ± 0.03	[74, 84]

Note. *a.* We list the parameters given from the GAUSS fit, by assuming one velocity component in the line of sight.

b. Lines are extracted from images by averaging a beam-sized region centered at P1 or S in the plane of the sky (Figure A1–A2).

All line images from the same species have the same pixel size and angular resolution (35.6'' for H₂CO and 33.9'' for CH₃OH).

c. Uncertainties on the measured intensities are typically $\leq 10\%$.

d. For line with $< 3\sigma$ emission, “---” is given in the line width, and a σ rms is given.

e. This column lists the velocity range we integrate for individual lines in order to estimate the molecular rotation temperature and column density using both RD and LVG fits.

f. The line shows emission with S/N < 4 toward S, so we do not use it for the RD or LVG fits.

g. At the rest frequency of 96.741 GHz, three transitions are blended in the velocity range of 65 ~ 90 km s⁻¹. In the velocity range where line wings of two transitions overlap, we assume that the transition with its line center close to the V_{lsr} dominates the integrated intensity. The velocity range over which we integrate each line is given with respect to the rest frequency of 96.741 GHz.

h. At the rest frequency of 157.270 GHz, three transitions are blended in the velocity range of 70 ~ 80 km s⁻¹. In the velocity range where line wings of two transitions overlap, we assume that the transition with its line center close to the V_{lsr} dominates the integrated intensity. The velocity range over which we integrate each line is given with respect to the rest frequency of 157.270 GHz.

i. The velocity range we select adds 20% uncertainty to the integrated intensity, but this is within the uncertainty from RD and LVG fits.

Table A3. Molecular column density toward P1, S, and Soff

Mol.	P1 (cm ⁻²) ^a	S (cm ⁻²) ^a	Soff (cm ⁻²) ^a
H ¹³ CN ^b	6.2 ± 1.4(12)	2.0 ± 0.7(12)	1.9 ± 0.7(12)
HC ¹⁵ N ^b	8.6 ± 3.7(11)	--	--
DCN ^b	1.8 ± 0.6(12)	0.9 ± 0.4(12)	1.1 ± 0.4(12)
HN ¹³ C ^b	5.8 ± 1.2(12)	3.1 ± 0.8(12)	3.6 ± 0.9(12)
H ¹⁵ NC ^b	7.0 ± 2.2(11)	3.3 ± 1.5(11)	4.4 ± 1.6(11)
DNC ^b	2.1 ± 0.6(12)	1.8 ± 0.5(12)	2.1 ± 0.6(12)
H ¹³ CO ^{+b}	3.2 ± 0.7(12)	1.9 ± 0.4(12)	1.7 ± 0.4(12)
HC ¹⁸ O ^{+b}	5.8 ± 1.6(11)	2.5 ± 1.0(11)	2.4 ± 1.0(11)
DCO ^{+b}	5.2 ± 1.3(11)	5.5 ± 1.4(11)	4.8 ± 1.2(11)
N ₂ H ^{+b}	3.4 ± 0.7(13)	1.5 ± 0.4(13)	1.7 ± 0.4(13)
N ₂ D ^{+b}	0.7 ± 0.3(12)	0.9 ± 0.3(12)	1.0 ± 0.3(12)
NH ₃ ^c	3.9 ± 2.6(15)	5.2 ± 4.2(15)	7.0 ± 5.6(15)
NH ₂ D ^d	2.7 ± 1.1(13)	2.2 ± 1.4(13)	2.1 ± 1.4(13)
CH ₃ OH ^e	2.8 ± 2.1(14)	0.6 ± 0.4(14)	0.6 ± 0.4(14)
CH ₂ DOH ^e	2.9 ± 1.7(13)	--	2.0 ± 1.0(13)

Note. *a.* Molecular column density is derived within a region with a radius of 5''

centered on P1, S, Soff, in the form of $x \pm y(z) = (x \pm y) \times 10^z \text{ cm}^{-2}$;

"--" stands for the intensity of $S/N < 3$.

b. Using T_{kin} derived from *p*-NH₃ (1,1) and (2,2) lines;

c. Assuming OPR of NH₃ is 1;

d. Assuming OPR of NH₂D is 3;

e. Using T_{rot} derived from the rotational diagram of CH₃OH lines.